This is to certify that the

dissertation entitled
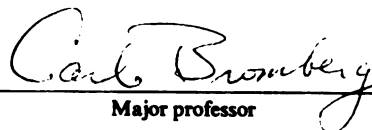
LARGE TRANSVERSE MOMENTUM
DIRECT PHOTON, π^0 AND η
PRODUCTION WITH A CARBON TARGET

presented by

Stephen R. W. Cooper

has been accepted towards fulfillment
of the requirements for

PhD degree in _Physics_

_____
Major professor

Carl Bromberg

Date _2/7/85_

0-12771

LARGE TRANSVERSE MOMENTUM
DIRECT PHOTON, π^0 AND η
PRODUCTION WITH A CARBON TARGET

By

Stephen R. W. Cooper

A DISSERTATION

Submitted to
Michigan State University
in partial fulfillment of the requirements
for the degree of

DOCTOR OF PHILOSOPHY

Department of Physics and Astronomy

1985

ABSTRACT

LARGE TRANSVERSE MOMENTUM
DIRECT PHOTON, π^0 AND η
PRODUCTION WITH A CARBON TARGET

By

Stephen R. W. Cooper

Measurements of direct photon, π^0 and η inclusive production cross sections have been made in a 200 GeV/c positive beam at FNAL. Data are presented for incident P and π^+ beams with a carbon target in the p_T range 2.05 to 5.00 GeV/c and the CM rapidity interval of -0.8 to 0.2. A liquid argon total absorption calorimeter was utilized as a photon detector.

The observation of a small but significant yield of direct photons is compatible with the predictions of Quantum Chromodynamics.

Dedicated to Robert Keith Cooper

who said I could.

ACKNOWLEDGMENTS

I would like to thank my advisor Professor Carl Bromberg for his sound teaching, enduring patience and wise advice.

I thank my wife Bonnie for staying with me and keeping my children well and happy throughout the years of my study.

I thank my father Dr. Willard G. Warrington for his help and good advice and my mother Janet Warrington for her love, inspiration and for her help in preparing figures for this document.

Finally I thank the Father, the Son and Holy Spirit for being with me.

TABLE OF CONTENTS

LIST OF TABLES

LIST OF FIGURES

4. Chapter 4 Figures

as dashed histograms. Background subtracted asymmetry distributions and Monte Carlo predictions (curves) for c) π^0 mass region and d) η mass region.

Chapter 1

Introduction

This chapter will outline the theoretical basis for the prediction and significance of direct photon production in strong interactions.

1.1 A Brief Parton Model Review

Quantum-electrodynamics (QED) has been shown to describe electromagnetic interactions to a very high degree of accuracy.[1] The success of QED has allowed the structure of hadrons to be probed in high energy experiments in which beams of electrons or muons are collided with hadronic targets. Results from these experiments, performed at SLAC, Brookhaven, Fermilab and CERN, have revealed the presence of structure within the proton. For example the high energy scaling behavior of the inclusive reactions ep→ex and μp→μx is in agreement with the predictions for the scattering of charged point particles. Using the results of these experiments and information taken from particle spectroscopy the presence of fractionaly charged,spin 1/2, point-like components or quarks (q) within the proton and neutron has been inferred.[2]

The experimentally observed scaling of deep inelastic charged lepton scattering has also suggested that in the fundamental interaction between a virtual photon and a quark, the quark behaves as if it were a free particle at high momentum transfers (asymptotic freedom[3]). In sharp contrast to this observation it has been impossible experimentally, to remove a quark from a hadron.[4] Instead, the final state quarks in charged lepton scattering appear to fragment into a "jet" of hadrons collinear with the direction of the virtual photon in the quark rest frame.[5,6] This, naively, contradictory evidence of quarks being free at small distances but unable to be separated to large distances, was an important clue in the development of the field theory for the strong interaction.

A further lead was obtained from measurements of proton quark probability distributions and momentum fractions derived from these experiments. They showed that only about 50% of the momentum of the target hadron is accounted for by quarks.[7] This signaled the presence of an electromagnetic neutral component, comprised of particles called gluons (g), carrying the balance of the momentum of a hadron.

Additional evidence suggested that the developing parton model of hadrons required a new quantum number. The spin 3/2 Δ^{++}-baryon with a valence quark assignment of three identical quarks in the same state was in conflict with spin statistics.[2] Also, QED predictions based on the parton model underestimated the lifetime of the π^0 by a factor of five.[8] Finally predictions of the ratio $\sigma(e^+e^- \to hadrons)/\sigma(e^+e^- \to \mu^+\mu^-)$ differed from the experimental values by factors of 2-3 depending on

the center of mass energy.[8] Each of these difficulties was removed by the introduction of a three-valued quantum number called "color".[2,8]

The evidence for quarks and gluons within hadronic matter outlined in Section 1.1, the large number of hadrons observed in experiments and the compelling evidence for the new color quantum number, led to the formulation of Quantum-Chromodynamics (QCD); a theory which describes hadrons and their interactions in terms of colored quarks bound together by a strong "color" force mediated by gluons.

1.2 Quantum-Chromodynamics   a Brief Review

In QCD, baryons are composed of 3 valence quarks while mesons are composed of a valence quark-antiquark pair.[9] Both baryons and mesons contain a small admixture of quark-antiquark pairs (sea quarks) in addition to their valence quark content.[10] The quarks come in various species (flavors), at this time all hadrons have been described with five flavors of quarks; u,d,s,c and b while at least one more flavor (t) is postulated[11]. The color force is associated with the color charge of the quarks,arbitrarily chosen to be Red, Blue and Green in an analogy with the three primary colors of light. Hadrons, which do not exhibit color charge, are assumed to be color-singlet combinations of the colored quarks; the analogy with light holds here as well, as Red+Blue+Green light appears as white (colorless) light. The color force is mediated by 8 massless gluons which simultaneously carry color and anti-color charge.

Since QCD is a field theory, many of the techniques of QED are directly applicable. In QED the elastic scattering of electrons requires the calculation of the effects of diagrams such as the one shown in Figure 1.1a. The elastic scattering of quarks, mediated by the exchange of gluons, requires the calculation of the effects of diagrams such as the one shown in Figure 1.1b. Due to the existence of the three gluon coupling, QCD requires the calculation of new diagrams such as the one shown in Figure 1.1c which are absent in QED. Another distinguishing characteristic of QCD is the dependence of the coupling constant on momentum transfer. In QED the effect of vacuum polarization loops (virtual photons that convert to virtual lepton anti-lepton pairs) is to surround each electric charge with a dielectric medium which in turn is polarized by and shields the electric charge. The canonical unit of electric charge measured by Millikan is observed for low Q^2 processes. At high Q^2 the polarized region filled with virtual lepton anti-lepton pairs surrounding each charge is penetrated and the unshielded "bare" charge is seen. This screening effect in QED is parameterized by a "running coupling constant" $\alpha(Q^2)$ as opposed to the classical constant coupling strength 1/137. Functionaly the QED "running coupling constant" diverges with increasing Q^2 but for all currently accessible energies is essentially 1/137. In QCD virtual gluons form quark anti-quark vacuum polarization loops that screen the color charge in analogous fashion to that described for QED. However, the gluon-gluon coupling results in vacuum polarization loops formed by gluon pairs. These gluon loops provide an anti-screening effect. The eight gluons that are possible as opposed to 6 quark flavors result in the gluon loops making a larger
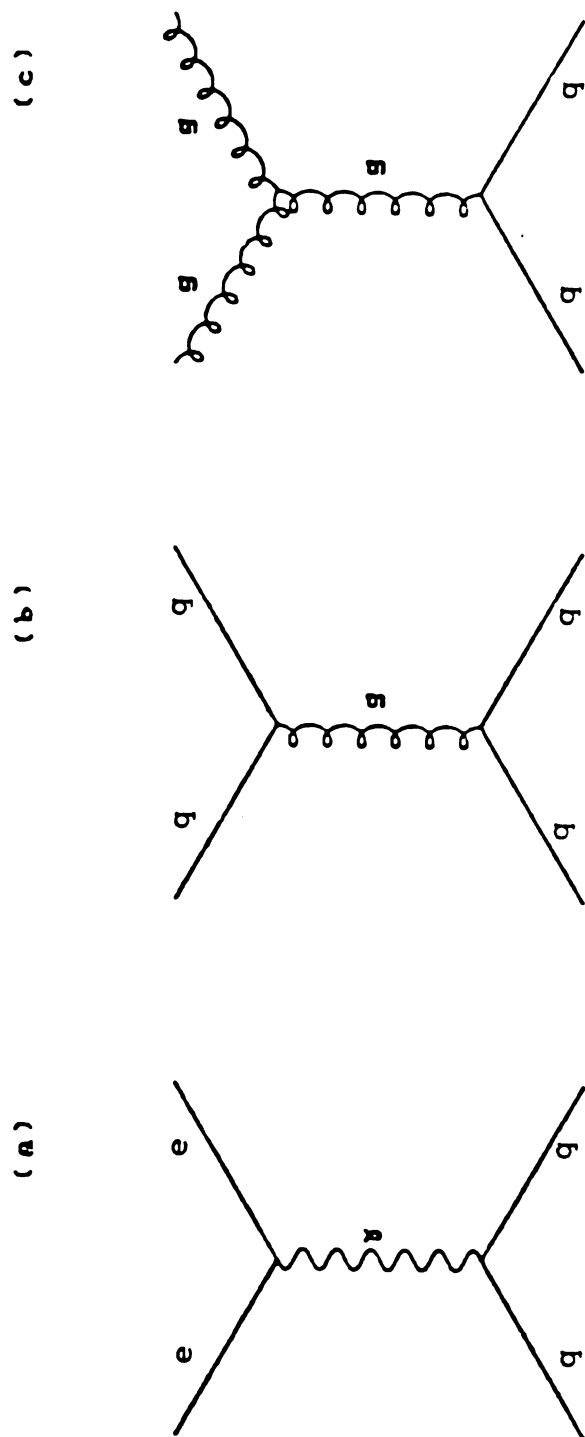
Figure 1.1; a) Photon exchange in the QED reaction, b) gluon exchange between colored quarks and c) quark gluon scattering via gluon exchange.

contribution than the quark anti-quark vacuum polarization loops.[2] The QCD running coupling constant as a result decreases for large Q^2 and increases for small Q^2. The anti-screening effect accounts for why quarks appear to behave as free particles at high Q^2, where $\alpha_s(Q^2)$ approaches zero, and yet cannot be separated beyond hadronic dimensions; at large distances the anti-screening yields an infinite color coupling which results in the "bremsstrahlung" of gluons and quarks ultimately forming a jet of hadrons.

1.3 High p_T Phenomenology

The parton model incorporating pointlike constituents within hadronic matter predicts the large angle scattering of the constituents. This leads to the production of large transverse momentum secondaries in high energy collisions. Early calculations based on QED interactions between partons predicted p_T^{-4} dependence for production above p_T 2 GeV/c.[12] Calculations using QCD to lowest order also predicted p_T^{-4} production.[13] Experimentally, hadron single particle cross sections decrease exponentially with increasing transverse momentum until 1 GeV/c. Cross sections at larger transverse momenta are much larger than predicted by an extrapolation of the low p_T exponential, however, a p_T^{-4} dependence is not observed.[8] In the p_T range 2-6 GeV/c the production cross sections varies as $(1-x_T)^{10} p_T^{-8.24}$, where the scaling variable x_T is the transverse momentum fraction p_T/p_{Tmax}. Recent experiments have found that for

$p_T > 6$ GeV/c and $x_T > .25$ the production data behave more like the p_T^{-4} behavior expected for point like scattering.[8] The implication is that for $p_T < 6$ GeV/c lowest order QCD processes are not adequate to describe the complete large p_T picture. For this reason tests of this theory are most easily done in reactions where large momentum transfers are assured. A number of theorists have suggested that the production of direct photons at sufficiently large p_T would be a ideal reaction for testing QCD.[14,15,16]

1.4 Direct Photon Production

Experimental tests of the fundamental quark-gluon interaction of QCD are fraught with difficulties. For one, the final state quarks and gluons of the process shown in Figures 1.1b-c are observed only indirectly through the hadronic jets into which they fragment. The detection and analysis of the hadronic jets that are produced by the scattered hadron quarks and gluons proved to be difficult for early experiments at fixed target machines.[17] Recently, experiments at CERN utilizing the large center of mass energies available in colliding beams have been successful in producing quantitative information on parton scattering at large transverse momentum.[18] However, it is still experimentally impossible to distinguish between quark and gluon jets.

In order to avoid this problem, and to select specific fundamental scattering processes we chose to exploit the fact that quarks through

their electric charge are able to couple directly to photons. In principle any reaction with a quark emitting a final state gluon can also proceed with a quark emitting a photon. Such photons would be "prompt" in that they would arise from the point-like coupling of the quark to the photon. In this fashion a final state photon with its well understood QED production mechanism replaces one of the final state jets of a purely quark-gluon interaction. The lowest order processes leading to the production of a direct photon at large transverse momentum (where perturbative QCD expansions are valid) are shown in Figures 1.2b and 1.2d (note that these Figures have a final state photon replacing a final state gluon in 1.2a and 1.2c).

Through these processes we hoped to test quark-gluon dynamics. Due to the statistical limitations of the data, we were unable to perform many of the tests of QCD possible with this reaction. For example the isolation and comparison of the processes in Figures 1.2c (Compton) and 1.2d (Annihilation) which have either a hard quark-gluon initial scattering with a quark jet in the final state (Compton) or a final state gluon jet (Annihilation) can probe the gluon structure function of hadrons and inspect the fragmentation function of scattered gluons. This comparison will be the subject of a new experiment to be performed at the Tevetron.

A competing mechanism to production via the Compton and Annihilation diagrams is "Final Bremsstrahlung" which is illustrated in Figures 1.2e-f. Upon inspection this process appears to be of higher order ($\alpha_s^2 \alpha$) than the Compton and Annihilation processes ($\alpha_s \alpha$).
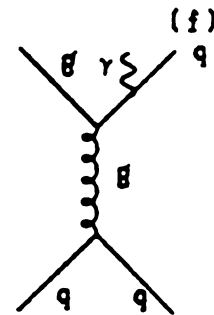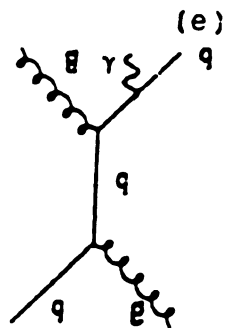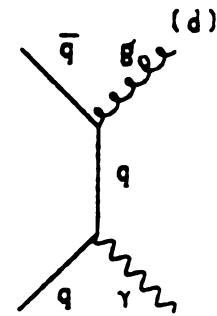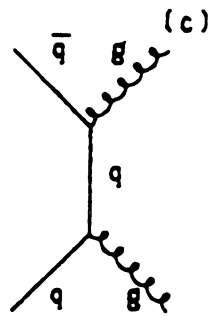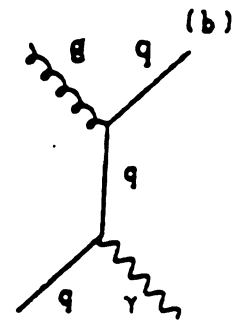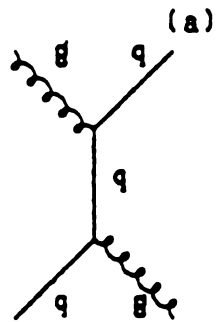
Figure 1.2; a) q+g→q+g b) q+g→q+γ (QCD Compton) c) q+q̄→g+g d) q+q̄→g+γ (Annihilation) e) q+g→q+g+γ (Brem.) f) q+q→q+q+γ (Brem.).

However, the fragmentation of quarks to photons is proportional to α/α_s resulting in the Bremsstrahlung processes being of order $(\alpha\alpha_s)$.[14]

Early calculations made for the p_T dependence of prompt photon production predicted a p_T^{-4} dependence at fixed x_T where an assumption of scaling in the structure functions was made.[14,15] Experiments to date have indicated a approximately p_T^{-6} dependence (this will be discussed in the final chapter). More recent calculations incorporating scaling violations (color force radiative corrections), a "running coupling constant" for the color force coupling and higher order production mechanisms have shown better agreement with data.[16,19]

For $pp \to \gamma + X$, $q\bar{q}$ annihilation would necessarily have to occur from the interaction of a sea antiquark with a valence or sea quark and therefore is suppressed relative to the Compton process. In $\pi^+ p$ and $\pi^+ n$ the annihilation of valence d quarks ($d\bar{d}$) can occur but does not compete with the Compton process due to the reduced charge coupling of d quarks to photons. Bremsstrahlung is expected to be important at large x_T values via the $q+q \to q+q+\gamma$ process but in the kinematic region covered in this experiment $.2 < x_T < .5$ Bremsstrahlung is estimated to occur at 30% of the Compton process.[20]

The experiment on which this dissertation is based searched for the presence of direct photons at large transverse momentum values between 2.0 and 5.0 GeV/c which are produced in collisions of 200 Gev/c proton and π^+ beams with a variety of nuclear targets (carbon, aluminum and

beryllium). Only the results obtained with a carbon target will be presented here. Nuclear target effects observed in this experiment are described elsewhere.[21]

Chapter 2

Experimental Apparatus

This chapter describes the experimental configuration used to measure the production of single photons at large transverse momentum (P_T) in Fermilab experiment E629.

2.1 Experimental Design and Components

Experiment E629 was conducted in the M-1 beam line of the Meson laboratory at Fermilab from the fall of 1981 through the spring of 1982. The collaboration for the experiment included physicists from Fermilab, Michigan State University, University of Minnesota, Northeastern University and University of Rochester.

The experiment used a beam line Cerenkov counter provided by Fermilab, a Beam-Hodoscope constructed by MSU, a Scintillator Counter Wall (80" X 40") provided by MSU, nine PWC planes constructed by University of Rochester,a Liquid Argon Calorimeter jointly constructed by University of Minnesota and University of Rochester, and a PDP-11

computer provided by Fermilab. The details of these components and their relationship to the experimental data are described in the following sections.

2.1.1 Targets, Beam and Interaction-Counters

Figure 2.1 shows the overall arrangement for E629. A Cerenkov counter upstream of the apparatus (not shown) was used to tag the beam (85% p, 15% π^+) as either a p or π^+. A unique scintillation counter hodoscope, detailed more fully in the next section, was placed in the beam line to generate a "Beam" signal. Two carbon blocks each of approximately 0.025 interaction lengths separated by 25 cm were used as targets. A target cave constructed of concrete shielding blocks surrounded the targets. Two scintillation counter pairs downstream of the target, each separated by 1" gaps centered on the beam line, were used to define an interaction in the target. One or more charged particles detected in one or more of these four counters in coincidence with a beam particle generated an "Interaction" signal. Various veto and halo scintillation counters suppressed triggers from the halo around the beam. A wall of eight 20" X 20" scintillation counters arranged in two rows of four that shadowed the electromagnetic shower detector was used to suppress triggers from particles produced by interactions upstream of the target. A signal from any one or more of the eight counters in the Veto-Wall generated a "Veto-Wall" signal. Similarly, a signal from either of the two Halo-Counters produced a "Halo" signal.
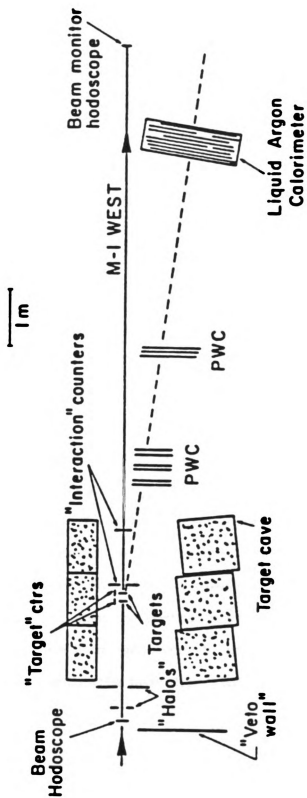
Figure 2.1; Layout of experiment E629.

2.1.2 Scintillation Counter Hodoscope

The experiment was designed to utilize an intense beam of 10^7 charged particles per second in order to access large p_T values where a direct photon signal could be separated from the background. For this beam a scintillation counter hodoscope[22] was designed and constructed at Michigan State University to provide (1) a monitor of the beam profile and beam intensity; (2) latched information on the beam position and multiplicity in each triggered event; and (3) fast signals to veto the presence of two or more beam particles within a single rf bucket (1 ns bursts, separated by 19 ns). The counters feature two staggered rows of scintillator elements, set in a precision mounting frame, which allows 100% coverage of the beam while limiting the overlap of adjacent elements to approximately 5% of the covered area.

In order to position the scintillator elements accurately to ±0.01 mm. precision slots were machined in a lucite window frame as shown in Figure 2.2a. Two frames, when bolted face to face, formed two rows of staggered elements as indicated in Figure 2.2b. The spacing of the slots was set such that adjacent elements would overlap by 0.02 mm. Eight 1 mm elements span the central portion of the hodoscope flanked on either side by one 2 mm and one 5 mm element. The slots are machined 2 mm in depth (the beam direction) to accept scintillators of this thickness.

a)

b)

1 mm

2 mm

BEAM
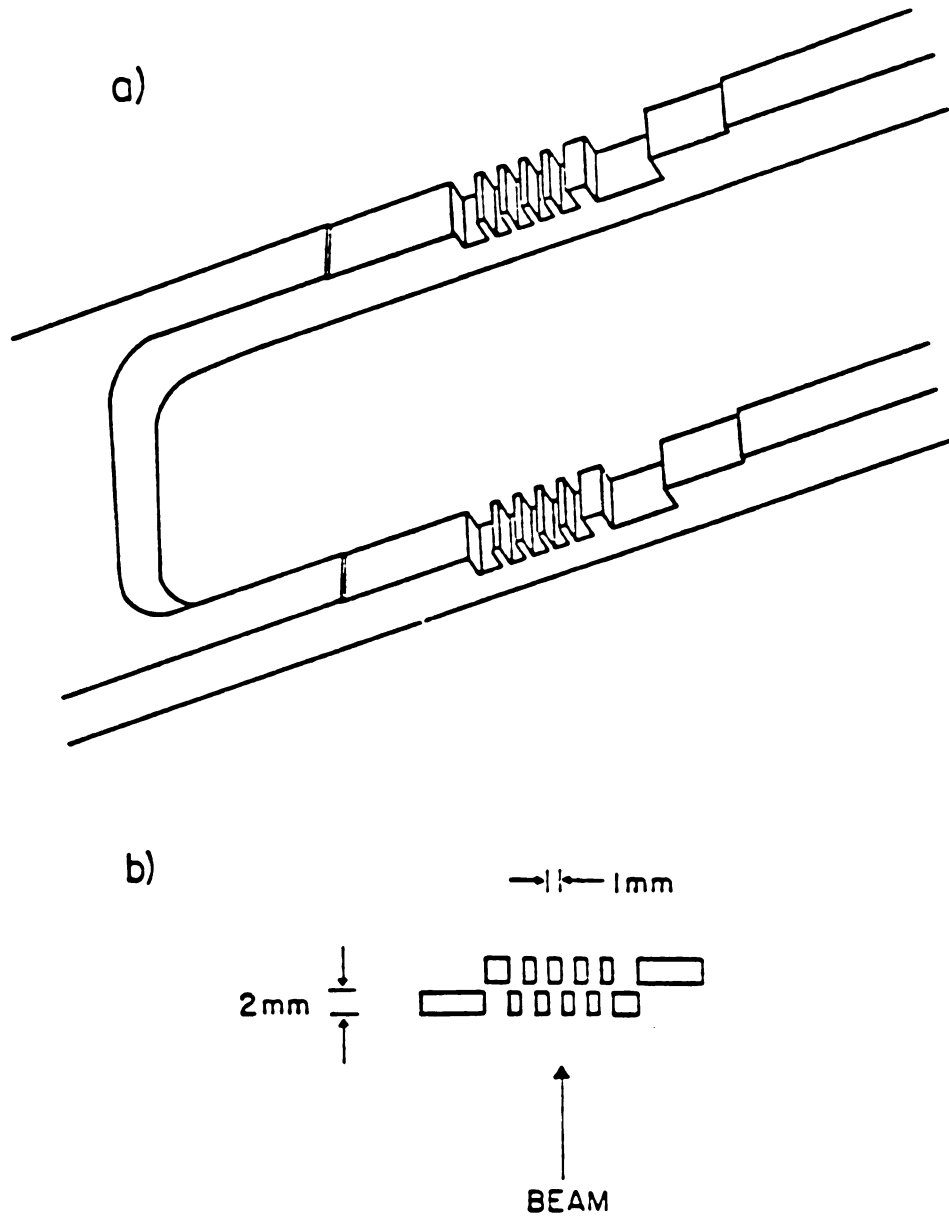
Figure 2.2; a) Lucite window frame for a hodoscope plane, b) end view of a complete hodoscope scintillator plane assembly.

The scintillators were wrapped with two layers of 0.008 mm aluminized mylar and sealed with a contact cement at one end and along the edge facing out from the slots. Approximately 3 mm of scintillator extended beyond the support frame allowing the light guides to be glued on. The light guides, of rectangular cross section, were tapered to approximately match the scintillator size on one end and the active area of the 1/2" diameter phototube on the other end. Before wrapping with aluminum foil and black tape, the light guides were heated and bent to shape in a jig in order to space the phototubes and bases as shown in Figure 2.3. Space limitations required that the six elements in one row be viewed from one side while the remaining six elements be viewed from the other side.

The scintillator support frame, phototubes, and bases were mounted on a 1/4" aluminum plate with a 6" square cut-out for the beam and halo. A light-tight box, through which the light guides penetrated, was also mounted on the aluminum plate.

Three hodoscope planes were built; two were placed just before the target (B_x, B_y) while a third (BV_x), was placed 10 m downstream of the target and used as a tag for a noninteracting beam track.

Measurements of the probability for greater than 1 element to be active at low beam intensities were consistent with the expected yield (5%) based upon the spatial overlap of neighboring elements. The increase in this probability at the nominal beam intensity

BASES

PHOTOTUBES

LIGHT GUIDES

SCINTILLATOR FRAME

←— 10cm —→
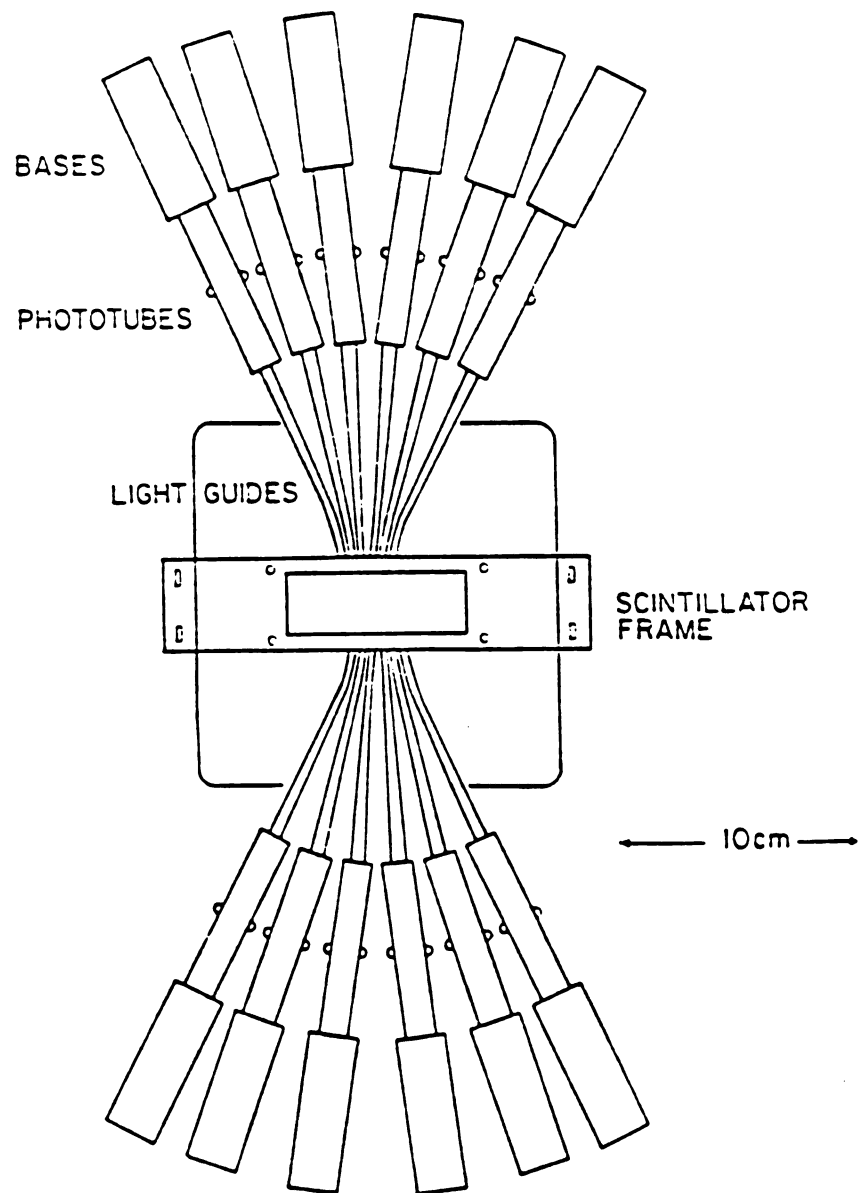
Figure 2.3; Complete hodoscope plane assembly.

(approximately 1 x10^7/s) agreed with that predicted from the beam structure. The efficiency of a plane was measured to be >98% indicating that few, if any, spaces were left between elements. At 10 MHz there was no indication of phototube gain sagging. During a particularly bad excursion in the beam intensity, 2.1 X 10^7 counts (twice the normal) were recorded during a single 1.0 s spill.

The signals from the 12 counters in each plane were discriminated and linearly summed to produce a final signal proportional to the number of hits in each plane. This signal was then discriminated at two different thresholds to differentiate between single and multiple hit events on each plane. The low threshold discriminator provided two signals, $B_x>0$ and $B_y>0$ indicating a hit in the x and y planes of the hodoscope respectively. The higher threshold discriminators produced two signals, $B_x>1$ and $B_y>1$ for the presence of multiple hits in the x or y planes.

2.1.3 Liquid Argon Calorimeter

The detector (LAC) was located 8 m from the target, and centered at an angle of 100 mr relative to the beam; at large p_T, this corresponds to production at 90° in the center of mass for this experiment. The theory of operation and the design details of similar detectors, have been described previously.[23]

Figure 2.4 shows an exploded view of the detector. It consisted of 61 lead sheets (2 mm thickness) and 62 copper-clad G-10 sheets
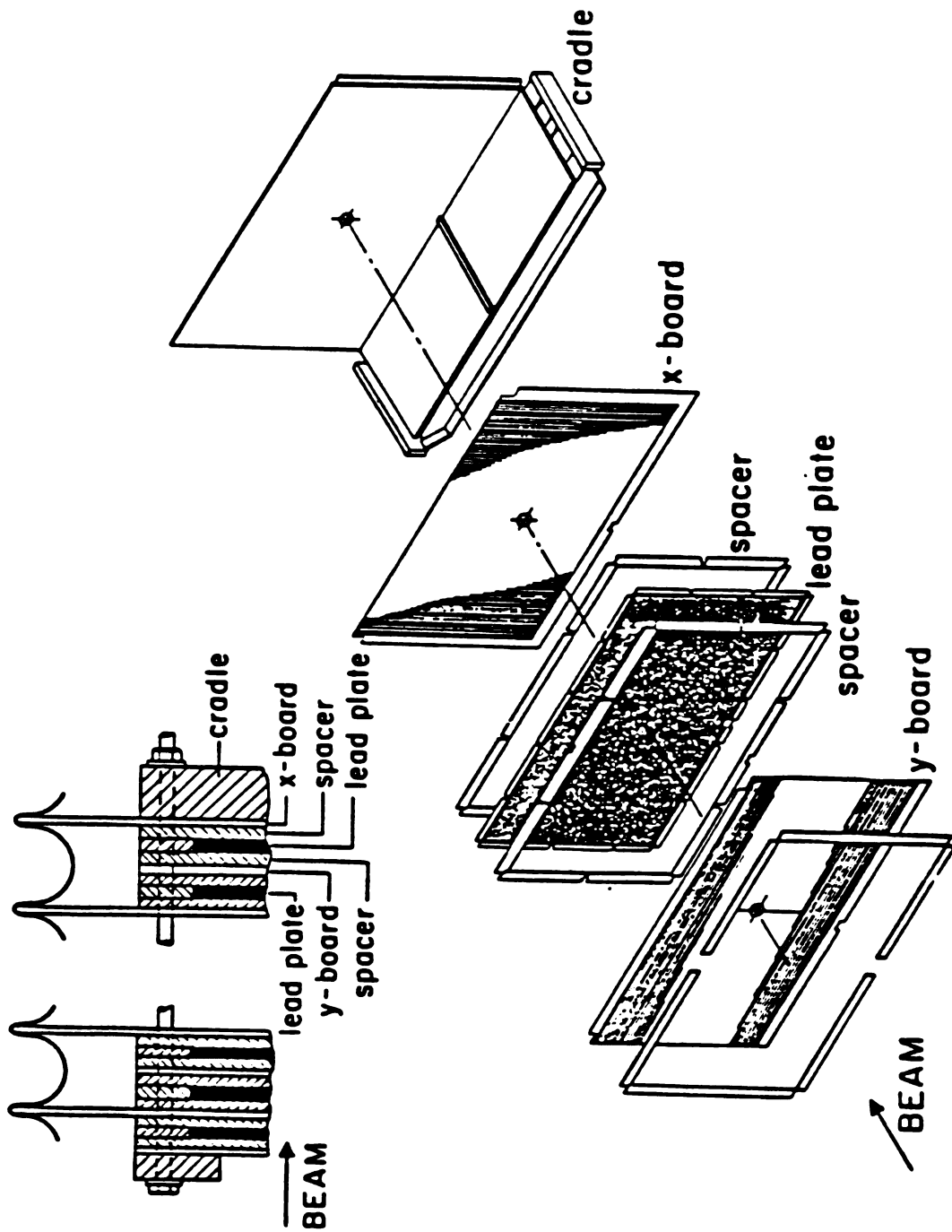
Figure 2.4; Exploded view of the Liquid Argon Calorimeter.

separated by G-10 spacers along the edges, and by small G-10 pins in the active area. The entire sandwich was held together and attached to its support structure by stainless steel rods. When immersed in liquid argon, the detector was 25 radiation-lengths and 1.2 pion interaction-lengths thick.

The copper-clad G-10 sheets were divided into strips 1.27 cm in pitch, with 0.5mm interstrip gaps. The strips extended along the X- and Y-directions on alternate sheets. The strips with same X and Y positions along the axis of the detector were connected to a single amplifier channel. However, the Y-measuring sheets were divided electrically into left and right sections, and the LAC read-out was further subdivided into front and back halves (each containing approximately 12 radiation lengths of material).

The detector-cradle assembly was suspended from a flat stainless-steel cover plate for the cylindrical cryostat (see Figure 2.5). This vacuum-insulated vessel was supported in a tall steel structure (tower).

Cryogenic temperatures were maintained in the vessel by sensing the liquid argon vapor pressure and controlling the flow of liquid nitrogen through internal cooling coils.

Figure 2.6a shows the block diagram of the front-end electronics for the detector.[24] The ganged strips from the detector were connected to individual amplifiers through multiconductor flat cables.
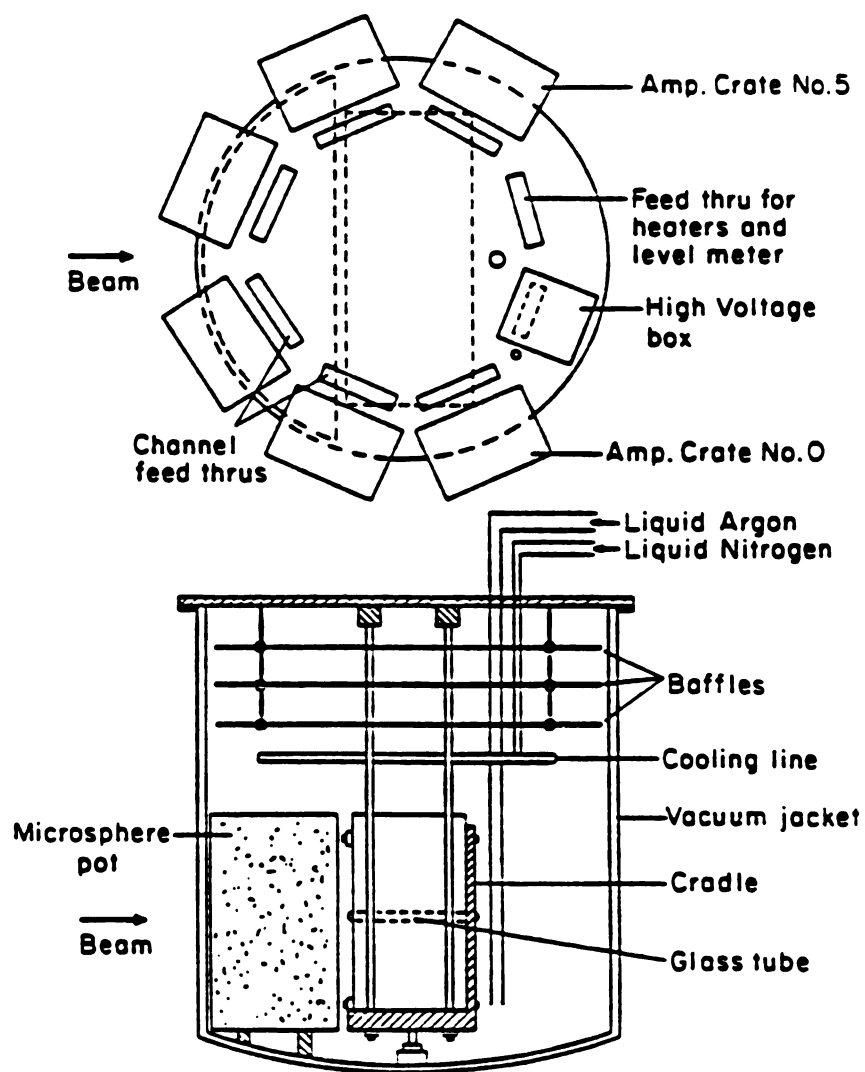
Figure 2.5; Calorimeter cover plate and cryogenic vessel.

a) Electronics for one channel of LAC

Difference Amplifier

Sample and Hold

SW1

SW2

© (c)

Delay Line

ⓑ (b)

Fast Trigger Amplifier

ⓐ (a)

Charge Sensitive Amplifier

Detector

b) Signal at point ©

Event of interest

SW1 opened

SW2 opened
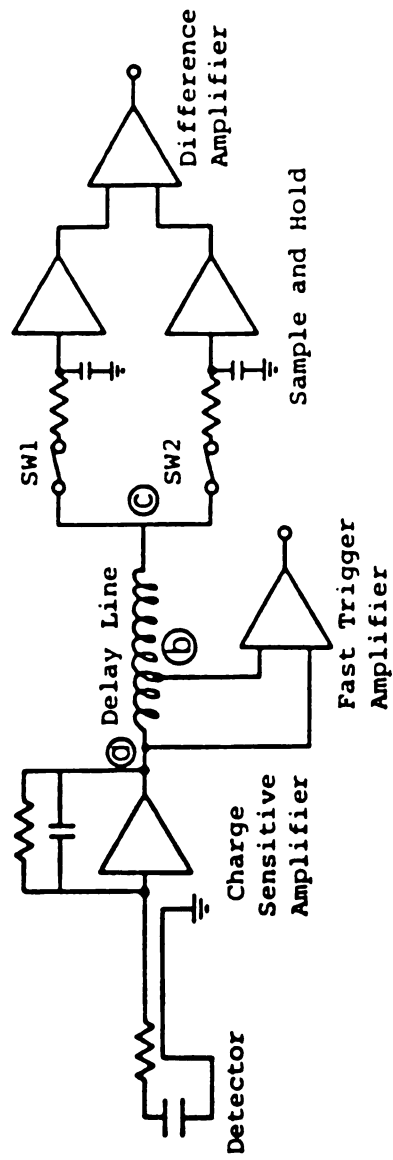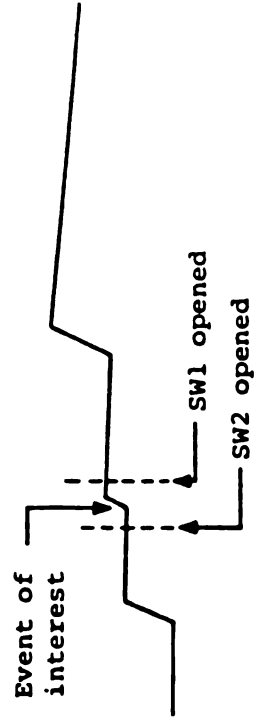
Figure 2.6; a) Electronics for one channel of the LAC b) signal sampling system.

A charge-sensitive and capacitively feedback amplifier was used. The amplifier output passed through a 400 ns lumped delay element to the sample-and-hold section. The CMOS switches SW1 and SW2 could be opened at the times appropriate for measuring the rise in the output for the event of interest as shown in Figure 2.1.6b, After both switches have opened, the output of the difference amplifier is proportional to the integrated charge for the event of interest.

In addition to the sample and hold section outputs, outputs for triggering purposes were provided by another difference amplifier driven by the front end. Baseline restoration was accomplished by delay-line differentiation using a 200 ns tap in the lumped delay element. The fast trigger outputs could be appropriately weighted, summed and discriminated to form an overall calorimeter trigger decision. The fast trigger outputs for all front x-strips were connected to low-threshold discriminators whose outputs went to time digitizers. The timing information later proved to be critical for the seperation of single photons from the background. A more complete description of the read-out electronics may be found elsewhere.[24]

A "Global-p_T" signal was formed with specialized electronics that added all of the x-strip energies from the fast trigger outputs. Each x-strip's fast trigger output was initially attenuated by a factor proportional to sin θ for that strip, where θ is the laboratory angle; i.e., Global-$p_T = \sum_{i=1}^{112} E_i \sin\theta_i$. The trigger threshold was later adjusted by modifying the attenuation factors in order to equalize the data accumulation rate across the detector. This resulted in an

effective threshold in p_T which varied from approximately 2.3 GeV/c at large angles, to approximately 3.0 GeV/c at small angles. This variation will be described in more detail in Section 3.3.1. The trigger reached nearly full efficiency approximately 0.5 GeV/c above the nominal threshold value.

In addition to Global-p_T, a "Local-p_T" signal was formed whenever at least 0.6 Gev/c was present in three neighboring x-strips. This served to suppress coherent noise and those multiphoton events in which there were no π^0 or η mesons produced with p_T above 1.2 Gev/c.

Operationally the Global-p_T discriminator threshold was set at 150 mV. This trigger setting was used for the majority of the E629 run time. Near the end of the run a dual threshold Global-p_T was installed. In the dual mode the 150 mV threshold signal was always enabled and the result latched. For 1 out of 3 events a 110 mV threshold signal was also enabled. In Section 3.3.1 a comparison is made between 110 mV threshold data where the 150 mV signal was, or was not, present in order to obtain the efficiency as a function of p_T for events requiring the 150 mv signal.

Not shown in Figure 2.1 was the proximity of power supplies (for beam line magnets) to the LAC. The Silicon Controlled Rectifiers (SCR's) in these power supplies induced electromagnetic pickup in the LAC. This noise produced levels above threshold in the Global-p_T signal with a duration on the order of 1-10 μs, and induced a strong background to the LAC p_T trigger. The SCR noise was characterized by a

bipolar oscillating signal. The negative part of the oscillation provided a signature for the presence of SCR noise. A signal gate was installed that would open whenever a Global-p_T pulse below -50 mV occured. The gate was continuously updated when additional negative pulses were encountered. Section 2.2.3 will describe how this gate was used to reduce SCR background signals to acceptable levels.

Due to restricted beam time at Fermilab in 1981, there was not sufficient time during the execution of E629 to calibrate the calorimeter using an electron beam. Instead the relative amplifier gains were measured by injecting pulses of fixed charge into the amplifiers. These results along with normalization to the π^0 mass provided the energy calibration for the experiment.[25] Photon reconstruction was accomplished by use of a program used in a previous experiment and modified for the E629 configuration. The reconstruction algorithm will be described in Section 3.1.

A more detailed description of the construction and performance of the LAC is available in a recent publication.[26]

2.2 Event Selection (Trigger)

As stated in Section 2.1, E629 was designed for a beam rate of approximately 10^7 Hz. The targets with a total of 0.05 interaction lengths yielded interactions at a rate of 10^6 Hz. The time required

for data acquisition limited E629 to a maximum of approximately 50 events to be recorded on magnetic tape per one second beam spill. The high event rate and relatively low data acquisition rate combined with the low rate expected for the production of high p_T photon events[27] required the formation of a highly selective trigger.

2.2.1 Pre-Trigger

The Global-p_T and Local-p_T signals in the LAC described in Section 2.1.3 had a rise time of approximately 200 ns. The PWC signals had a rise time of approximately 20 ns and a duration of 60 ns. Delaying the PWC signals long enough to include LAC information in a latch decision (> 100 ns) was impractical, this resulted in the need for a early or "Pre-Trigger" for the PWC latch decision.

A Pre-Trigger was formed when both the $B_x > 0$ and $B_y > 0$ hodoscope signals were in coincidence with the Interaction signal and a "Computer-Ready" signal which indicated the computer was free to record data. A coincidence with both the $B_x > 1$ and $B_y > 1$ signals or the Halo signal would veto the formation of a Pre-Trigger. The logic is summarized as follows:

$$\text{Pre-Trigger} = (B_x > 0) \cdot (B_y > 0) \cdot (\text{Computer-Ready}) \cdot \overline{(B_x > 1 \cdot B_y > 1)} \cdot$$
$$(\text{Interaction signal}) \cdot \overline{(\text{Halo signal})}.$$

When a Pre-Trigger was formed, a latch was set that prevented the formation of subsequent Pre-Triggers until cleared. The resulting dead time between the Pre-Trigger formation and the interrogation of the LAC was continuously monitored by counting beam in scalers which were gated off when the Pre-Trigger latch was set.

2.2.2 Kill-Latch

The long response time of the LAC, approximately 400 ns as described in Section 2.1.3, implies that contamination of a given event by preceding and succeeding events is possible. In order to protect the trigger from pile-up, any one of three states to be described would set a "Kill" latch which would block the formation of a Final-Trigger until cleared.

Two of the "kills" used an Interacting-Beam signal (IB) formed by the coincidence between the $B_x{>}0$ and $B_y{>}0$ Hodoscope signals and the Interaction signal. An IB signal occurring up to 100 ns prior to the event being processed would generate an "Early-Kill". A "Late-Kill" was formed if a IB signal occured up to 75 ns after the event being processed. The "Veto-Wall/Halo-Kill" occured when a Veto-Wall or Halo signal occured up to 100 ns before or approximately 50 ns after the event being processed. These pile-up protections had a dramatic effect on the large p_T trigger rate. Prior to their introduction the trigger rate (triggers/beam particle) was linearly proportional to the beam

intensity. Following their introduction the trigger rate was independent of the beam intensity.

2.2.3 Final-Trigger

The Pre-Trigger signal indicated that a single beam particle had interacted in the target and that the computer was ready to accept data. If the Kill latch was not set the event was isolated in time. The Global-p_T and Local-p_T signals then provided information on the probable presence of high p_T photons. The Final-Trigger was formed by requiring a coincidence between the Pre-Trigger, Global-p_T and Local-p_T signals with the SCR and Kill signals acting in veto. The logic can be summarized of follows:

$$\text{Final-Trigger} = (\text{Pre-Trigger}) \cdot (\text{Global-}p_T) \cdot$$
$$(\text{Local-}p_T) \cdot \overline{(\text{SCR})} \cdot \overline{(\text{Kill})}.$$

An event satisfying the Final-Trigger initiated the sample and hold, digitizing and read-out procedures of the LAC under computer control. When an event failed to satisfy the Final-Trigger requirement an appropriately delayed Pre-Trigger signal cleared all latches to be ready for the next event.

Chapter 3

Data Characteristics

This chapter will detail the procedures used to reconstruct photon positions and energies, to remove spurious sources of photons from the raw data and to parameterize the acceptance of the detector.

3.1   Photon Reconstruction

The LAC construction, as described in Section 2.1.3, provided x and y views of the energy deposition profiles of electromagnetic showers. The longitudinal division of photon energy into front and back energies was also described.

In the first stage of photon reconstruction the x(front) and y(front) views are independently analyzed for possible electromagnetic showers. Figure 3.1 displays a typical view containing three "groups" of energy (A,B and C), where a group is defined as one or more consecutive read-out strips with energy depositions above threshold (threshold=.10 GeV). Each group is then analyzed for peaks; any strip
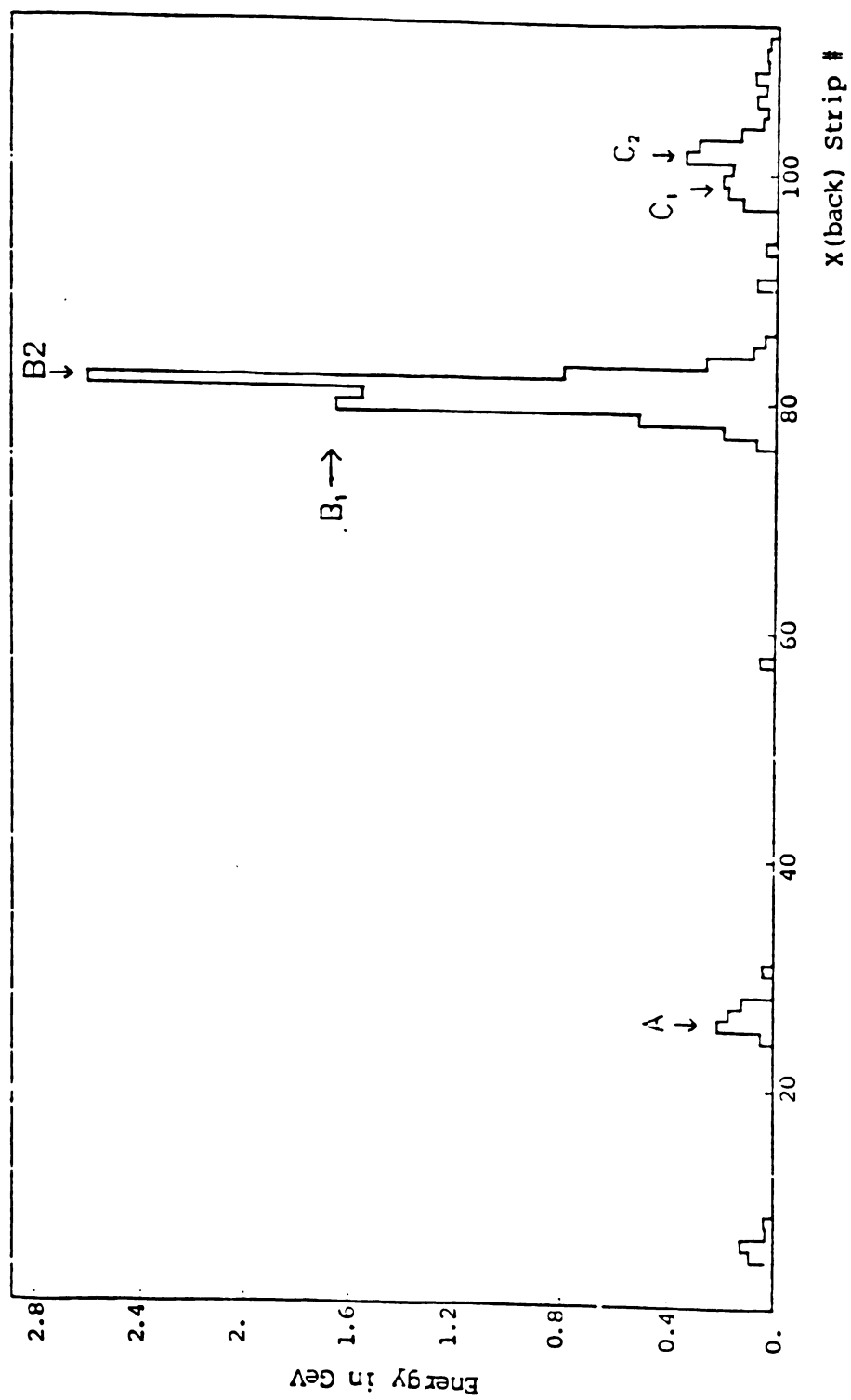
Figure 3.1; An energy deposition profile in the x view showing five peaks; A, B_1, B_2, C_1 and C_2.

in a group with a higher energy than its adjacent strips is defined as a peak.   In the figure groups B and C have two peaks each and group A has one peak. In subsequent analysis B1 and B2 were interpreted as the x-view of showers from two separate photons with a combined effective mass of .136 GeV/c^2 indicating a possible π^0 (see chapter 4).

The interleaving of x and y signal planes in the LAC as described in Section 2.1.3 results in a near equivalence between the x and y views of a electromagnetic shower in the front and in the back segments of the detector.

In order to illustrate the character of the data analysis a breakdown of the steps involved in the reconstruction of two events will be given. The four views of an uncharacteristically simple event are shown in Figure 3.2. A single group with only one peak is seen in each view. The energies of the front groups are 5.51±0.33 GeV and 4.76±0.31 GeV located at strips 22 and 44 in the x and y views respectively. The energies in the back views are 1.26±0.16 GeV and 1.48±0.17 GeV and are located at strips 21 and 44 in the x and y views respectively. After a summation and correction for shower shapes of the energies in each view this event was interpreted as an isolated photon with an energy of 12.5±0.49 GeV, located at strip numbers x=22 and y=44 with p$_T$=2.49±0.22 GeV/c. Subsequent use of a shower shape parameterization allows the spatial position to be determined within σ=.7mm for any given view.[28] Note also that the energy in the back is centered at nearly the same x and y positions as the front energies indicating a nearly normal incidence for the photon. The dotted line

33
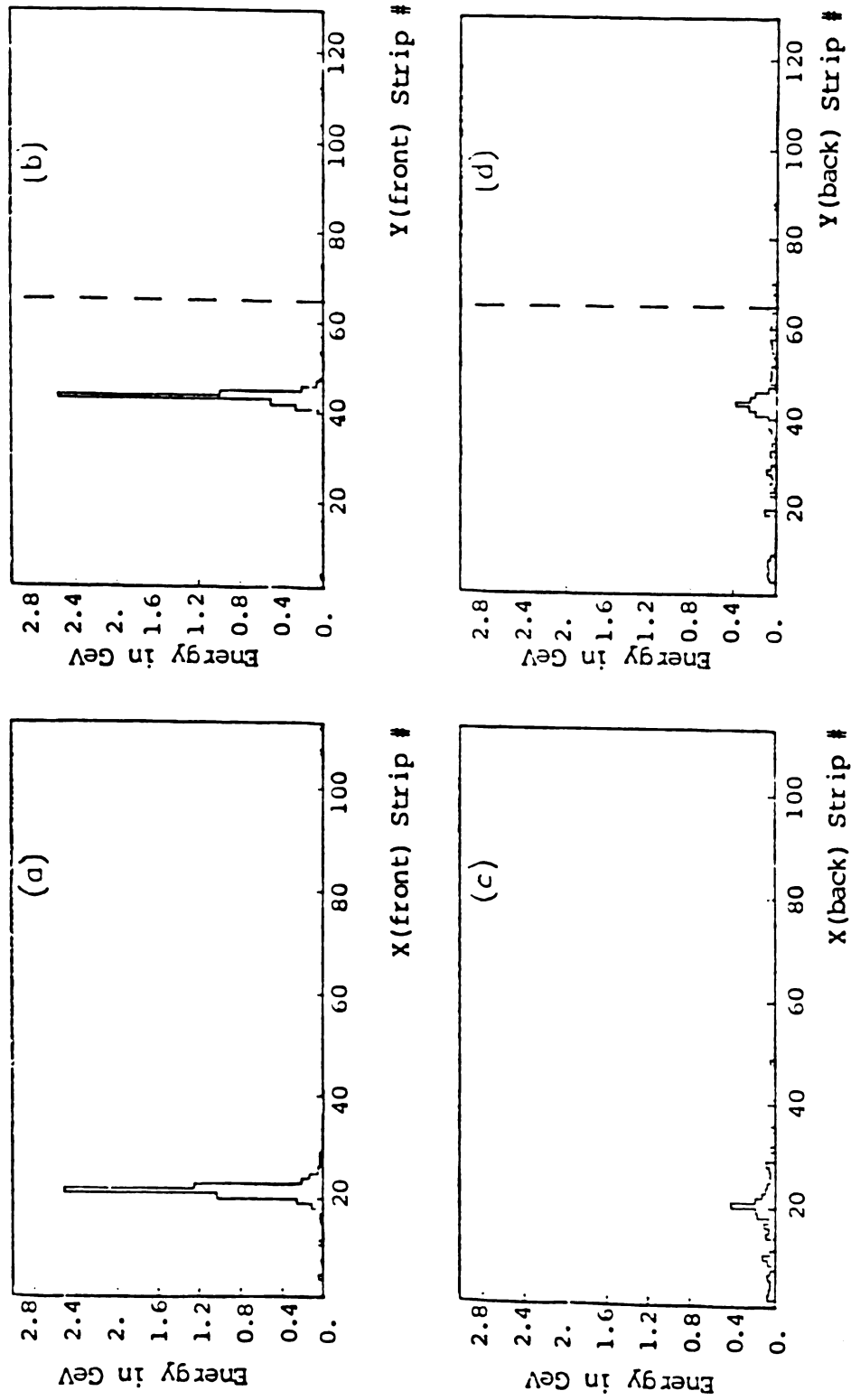
Figure 3.2: The X(front), Y(front), X(back) and Y(back) views (a-d respectively) of a 1 photon event with energies of 5.51, 4.76, 1.26 and 1.48 GeV respectively.

in the y plots delineates the electrical division of the y-strips into left and right sections as described in Section 2.1.3. This results in y-strip k, where $1 \leq k \leq 64$, having the same y position as y-strip k+64.

In events with more than one photon incident on the detector, position ambiguities are resolved by direct energy matching. An event in which two photons were reconstructed is shown in Figure 3.3. The energies and positions for the groups in each view are given in Table 3.1.

Table 3.1; Energies and positions of groups in a 2 photon event.

x Group	xfl	xf2	xb
E (GeV)	6.66±0.36	2.31±0.21	2.36±0.22
x-strip#	52	58	52
y Group	yfl	yf2	yb
E (GeV)	6.73±0.36	1.73±0.18	1.82±0.19
y-strip#	23	79	23

Each group contains a single peak which can be unambiguously paired by energy matching. In the front section groups xfl and yfl are nearly equal in energy as are groups xf2 and yf2. Similarly, in the back, xb and yb are nearly equivalent in energy. By assuming near normal incidence for photons, xb and yb can be associated with xfl and yfl respectively. Summing the x,y, and back energies of the associated groups the two clearly indicated photons are reconstructed with energies of 17.71±0.59 and 4.62±0.30 GeV located at strip coordinates (52,23) and (58,79) respectively. Note that only the large energy photon is associated with energy in the back views of the event; it is
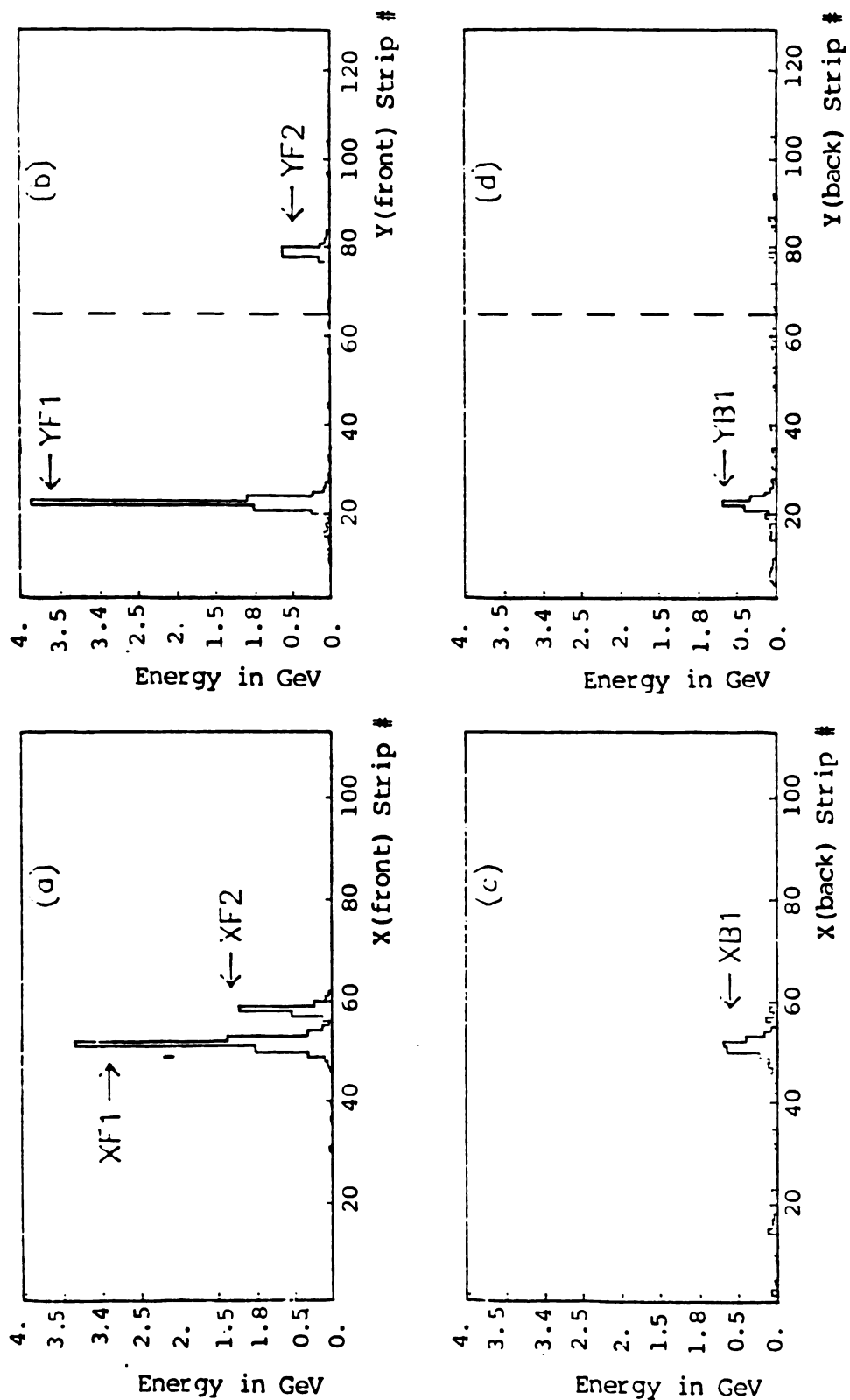
Figure 3.3: The X(front), Y(front), X(back) and Y(back) views (a-d respectively) of a 2 photon event with group energies of 6.66 and 2.31 GeV in X(front) and 6.73 and 1.73 GeV in Y(front). In the back views only the first photon is visible as a peak with group energy 2.36 GeV in X(back) and 1.82 GeV in Y(back).

indicated, therefore, that the lower energy photon did not deposit a significant fraction of its energy in the rear section. The effective mass of the two photons is .141 GeV/c^2 indicating a possible π^0 and the P_T of the two photons together is 3.44 GeV/c.

The two events just examined were chosen because of their straightforward interpretation. In cases where the electromagnetic showers overlap in one or more views or the energies of photons are nearly equal, resolution of the ambiguities in view matching requires specialized coding. Shower shape parameterizations were used to partition the energy in multiple peak groups between the overlaping showers.[28] Reconstruction of special cases with complications beyond those just mentioned are also present. However,as they apply only to limited class of events, they are not individually treated here.[29] A 1 GeV minimum energy requirement resulted in a average reconstructed photon multiplicity of 4.4. The effectiveness of the reconstruction is demonstrated by the 2γ mass spectra shown in Figure 3.4 with a P_T cut of 2.5 GeV/c. Every 2γ combination is included and clear π^0 and η signals are in all but the highest multiplicities where only the π^0 is evident.

A Monte Carlo study was used to determine the γ, π^0 and η reconstruction efficiencies. The results of this study are used later in Section 4.3.1 to correct for contamination in the direct photon signal.
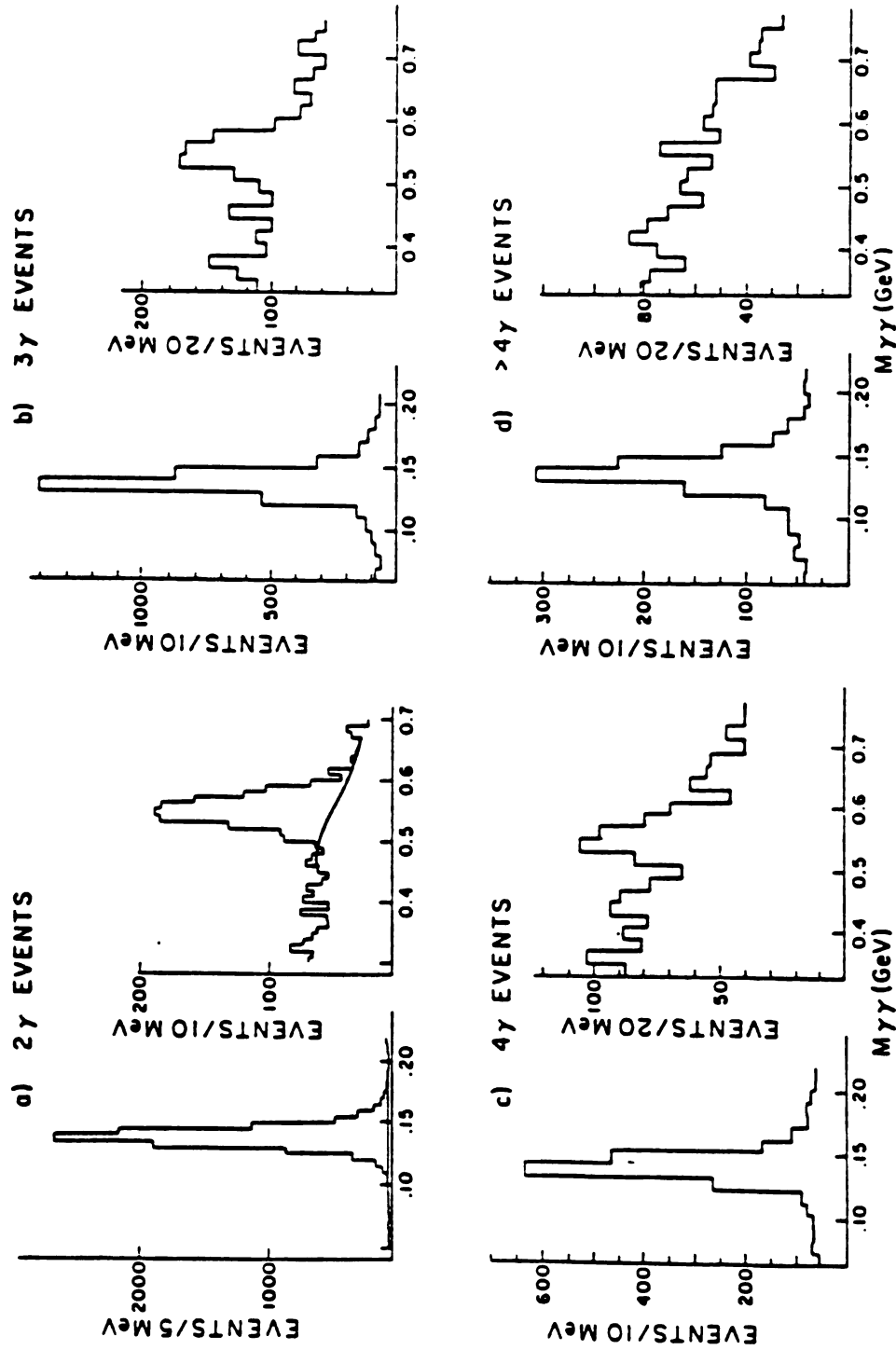
Figure 3.4: 2γ Effective mass of all 2γ combinations with $P_T > 2.5$ GeV/c for a) 2γ events b) 3γ events c) 4γ events and d) > 4γ events.

3.2 Identification of target and beam associated events

The experimental trigger was designed to select interactions in the target yielding a large p_T electromagnetic energy deposition in the LAC. Triggers due to energy depositions from beam halo, hadronic interactions in the LAC and pile-up from previous and subsequent interactions were removed from the data by applying cuts on the time, direction and the energy deposition characteristics of each event. These cuts are described fully in the following sections.

3.2.1 Time Cut

As described in Section 2.1.3 the x-strip read-outs in the first 12.5 radiation lengths of the LAC were provided with low threshold discriminators; each discriminator output was used as the start signal for a time-to-digital converter (TDC). An appropriately delayed interaction signal provided the common stop signal for all channels (See Section 2.1.1). The signal on an individual LAC strip had a typical rise time of approximately 200 ns as described in Section 2.1.3. A true target associated signal in any given LAC strip should have a fixed TDC result (prompt time) due to the time-of-flight, the intrinsic delay due to cabling, and the delays in the other associated electronics. However, due to the fact that signals with a fixed rise time cross a given threshold at times which are a function of the ultimate signal height, the actual TDC result for in-time events varied from the prompt time. This time-slewing is exhibited in Figure 3.5
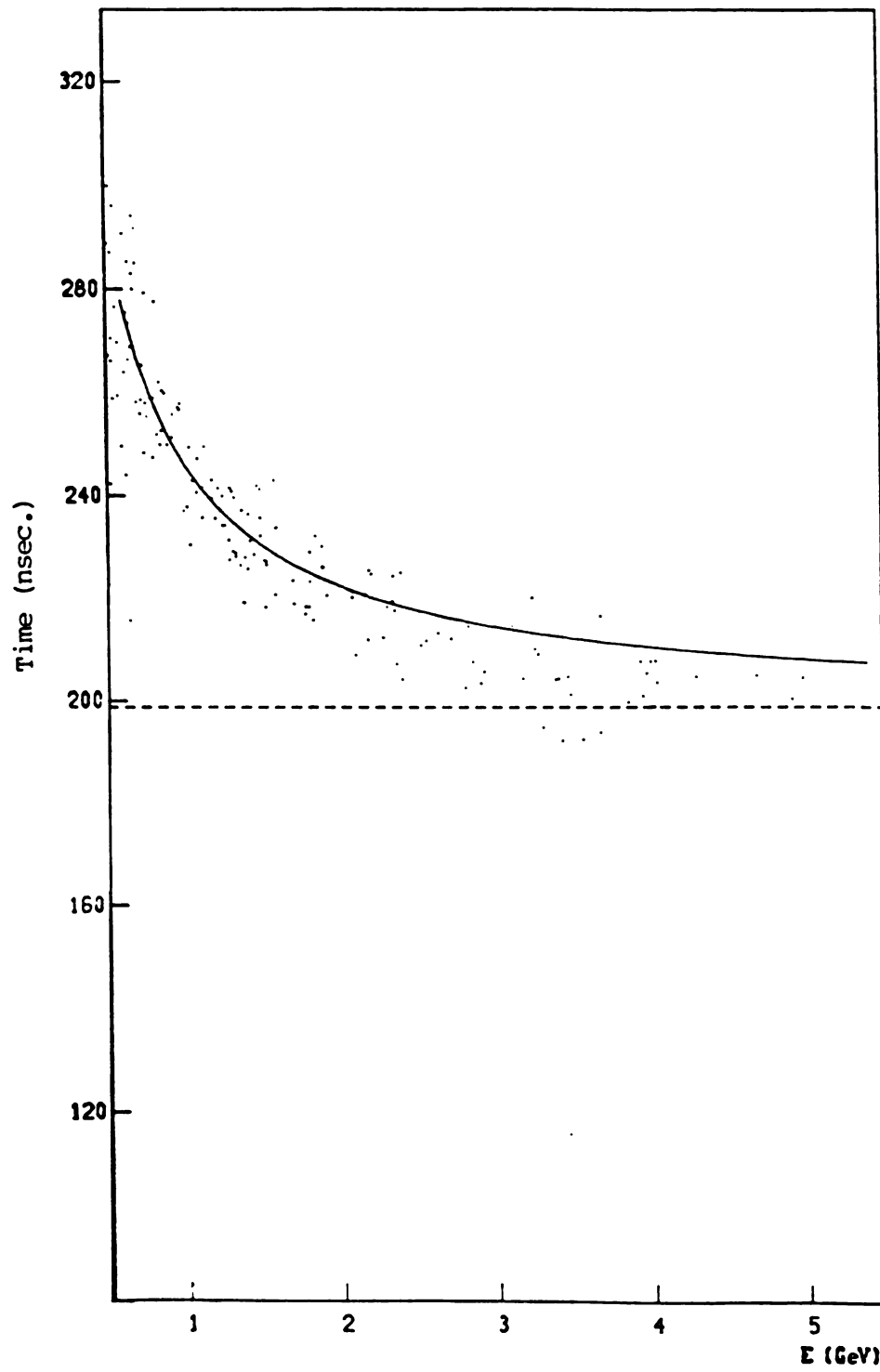
Figure 3.5; Time vs. energy for X(front) Strip 93.

where a scatter plot of strip time vs energy is shown for x-strip 93; in order to insure a high proportion of in-time events the timing analysis was restricted to entries taken only from photons that formed a π^0. The prompt or minimum response time is indicated by the dashed line in the plot. The solid curve shown on the plot is of the form (energy)$^{-1}$ times a scale factor plus an offset (see Appendix A). A scale factor and offset were determined for each x-strip. Corrected strip times were then taken as the difference between the original time and a time calculated on the basis of the relationship just described. Prompt events in this regime have a corrected or prompt time of Zero.

Energy weighted averages of the corrected strip times were used to determine a time for each shower. The time spectrum of photons from single photon triggers is shown in Figure 3.6. The structure in the tail of the in-time peak reflects the 19ns rf bucket structure of the FNAL accelerator (see Section 3.2.2). In subsequent analysis a time cut of ±25ns was applied to the highest energy photon in each event.

3.2.2 Direction Cut

The front and back segmentation of the detector provided a method of differentiating between events originating in the target from those originating elsewhere. The method is demonstrated with Figure 3.7. A photon from the target, traveling along the dashed line, deposits most of its energy in the front half of the detector at position X_F, and the
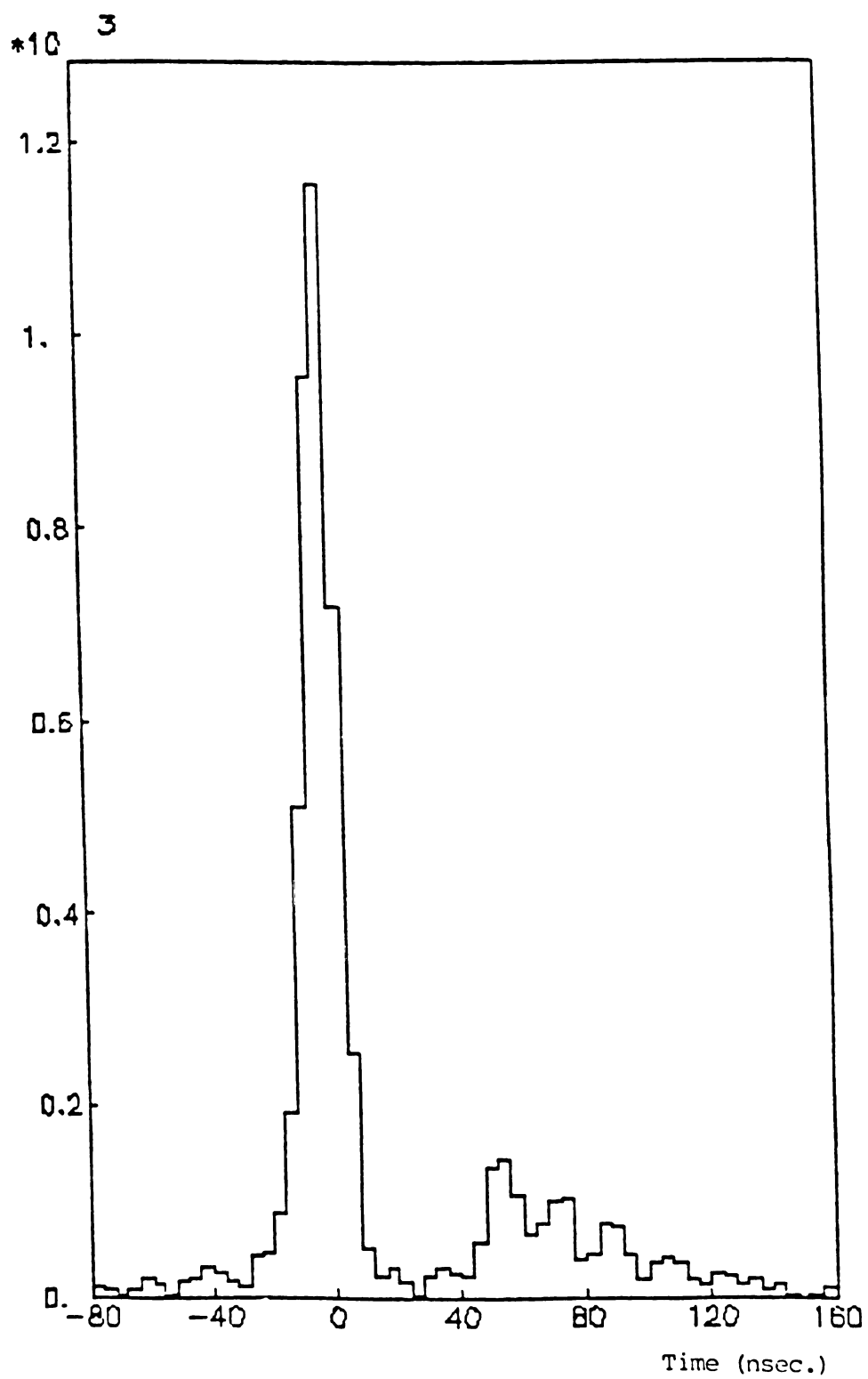
Figure 3.6; Timing spectra for single photon triggers with pT > 2.0 GeV/c.

$$\Delta X_B = \frac{T_{LAC}}{D_{LAC}}(X_F - X_0)$$
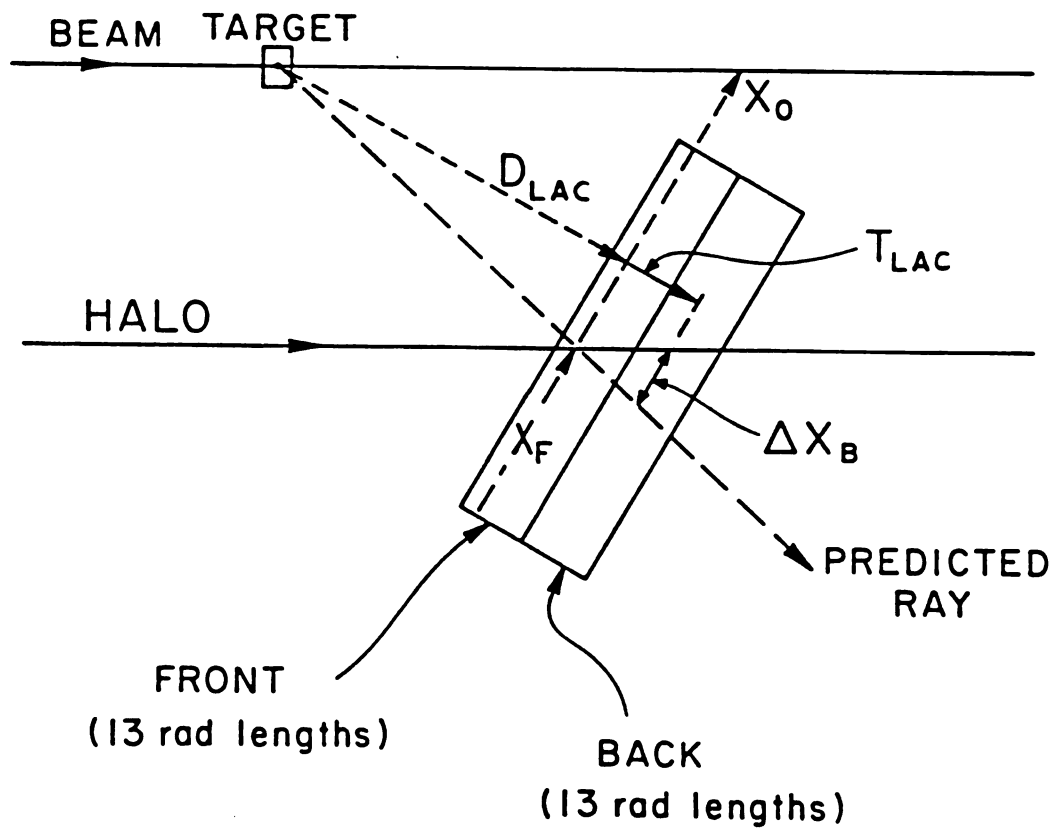
Figure 3.7; Angular orientation of the LAC.

remainder in the back half directly behind X_F. For a photon traveling parallel to the beam direction and striking X_F the back energy is displaced from the expected position ΔX_B. The ΔX_B distribution for photons that originate in the target is centered at zero. Figure 3.8 is a scatter plot of ΔX_B versus X_F for events in which only one photon was found in the detector. Two distinct bands are present: one, corresponding to sources from the target, centered at $\Delta X_B = 0$ (independent of X_F), and another tilted relative to $\Delta X_F = 0$. The tilted band is that expected for the dependence of ΔX_B on X_F for photons or hadrons traveling parallel to the beam direction. (The two horizontal gaps are due to dead amplifiers in several of the back x-strips.) Taking the rms width of the central peak, and estimating the effective lever arm between the front and back of the LAC, we find an angular resolution for determining the directions of incident photons of ±30 mr (rms).

The combined effect of both the direction and the time cuts is shown in Figure 3.9 where those events passing the direction cut are indicated by the shaded portion of the plot. In the p_T ranges 2-3 and 3-4 GeV/c, the vast majority of the photons in the central in-time peak also satisfy the direction cut. In the p_T range greater than 4 GeV/c the application of the direction cut in conjunction with the time cut, which are both effective at removing halo backgrounds, leaves a clean sample (shaded events at t=0) of single photons originating from, and in coincidence with a beam interaction in the target. The veto wall protection described in Section 2.2.2 is clearly evident in Figure 3.9c as is the the 19 ns rf bucket structure of the FNAL accelerator.
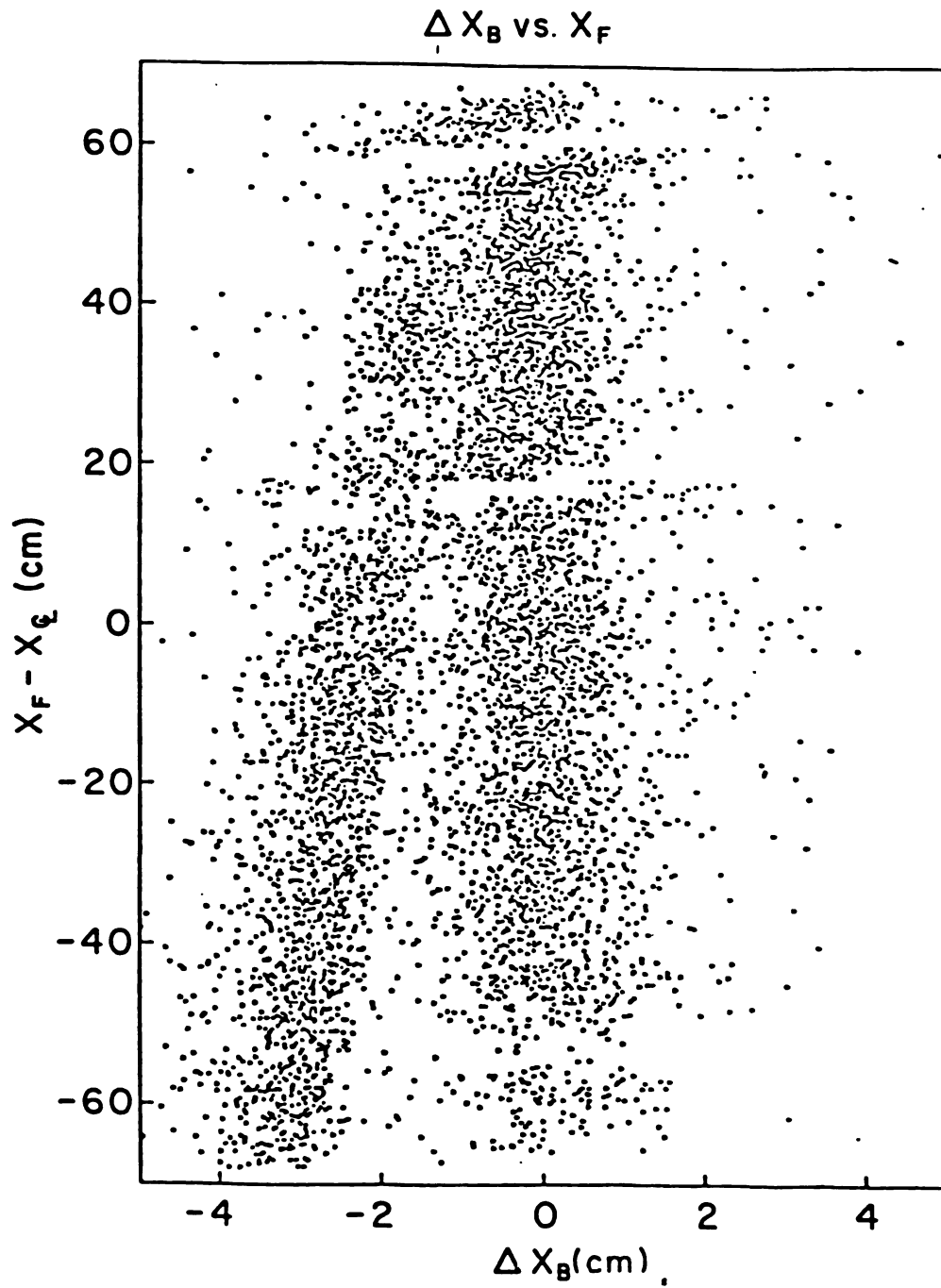
Figure 3.8; Off Axis ($\Delta X_B \neq 0$) and target associated ($\Delta X_B \simeq 0$) photons.
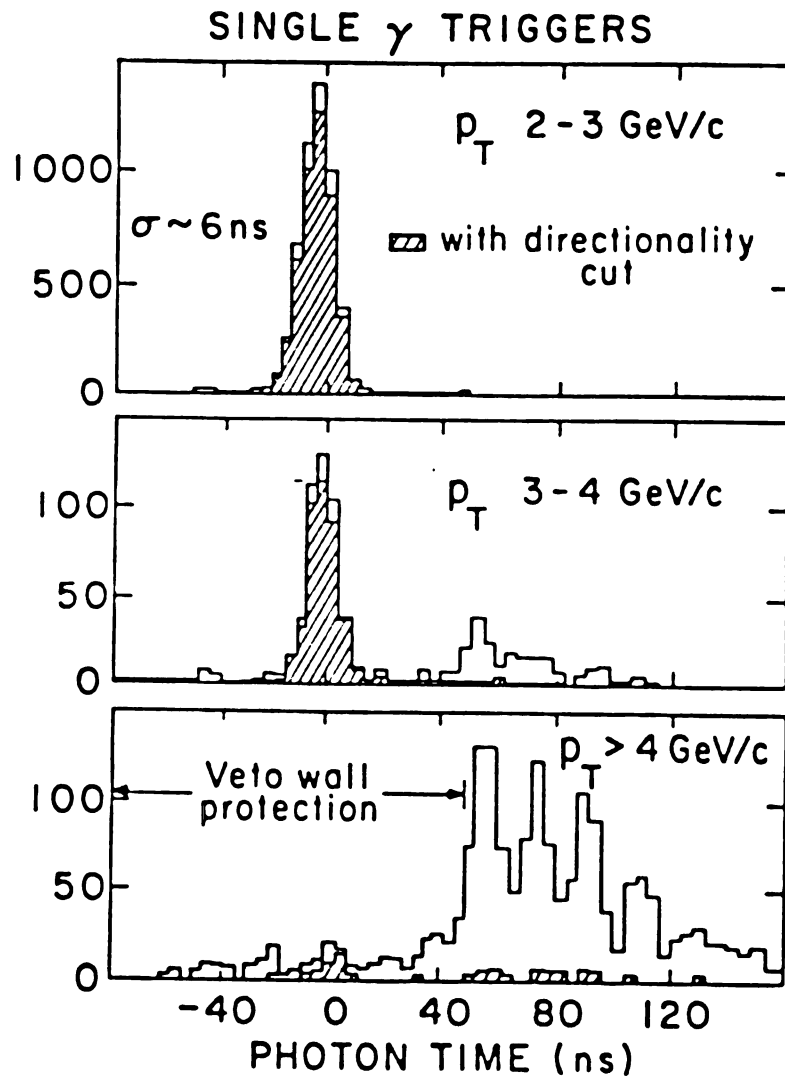
Figure 3.9; Timing spectra for single γ triggers.

3.2.3 Hadron Cut

The difference in response of the LAC to hadron-induced showers and to electromagnetic showers provided a basis for eliminating hadron induced triggers. As noted in Section 2.1.3 the LAC had a thickness of 25 radiation lengths, but only 1.2 interaction lengths. The fraction of pions which deposit more than a given percentage of their total energy in the LAC is shown in Figure 3.10a.[30] Less than 20% of all hadrons will deposit greater than 50% of their energy in the LAC. This results in a strong suppression of large p_T hadronic triggers due to the steeply falling cross sections with increasing p_T. The fractions of pions and electrons (equivalent to photons) which deposit less than a given percentage of their total energy in the back half of the LAC is shown in Figure 3.10b (the 30% of the pions which deposit less than 10% of their total energy in the LAC have been excluded). The cut on E_{BACK}/E_{LAC} of 0.5 which was applied to the largest energy shower in each event eliminated 55% of pion-induced showers (mislabeled as electromagnetic), with a negligible effect on photons. When considered in combination with the consequences of Figure 3.10a, it is clear that the LAC provides excellent discrimination against hadron background to high-energy photons. The small residual hadronic background is discussed in Section 4.3.4.
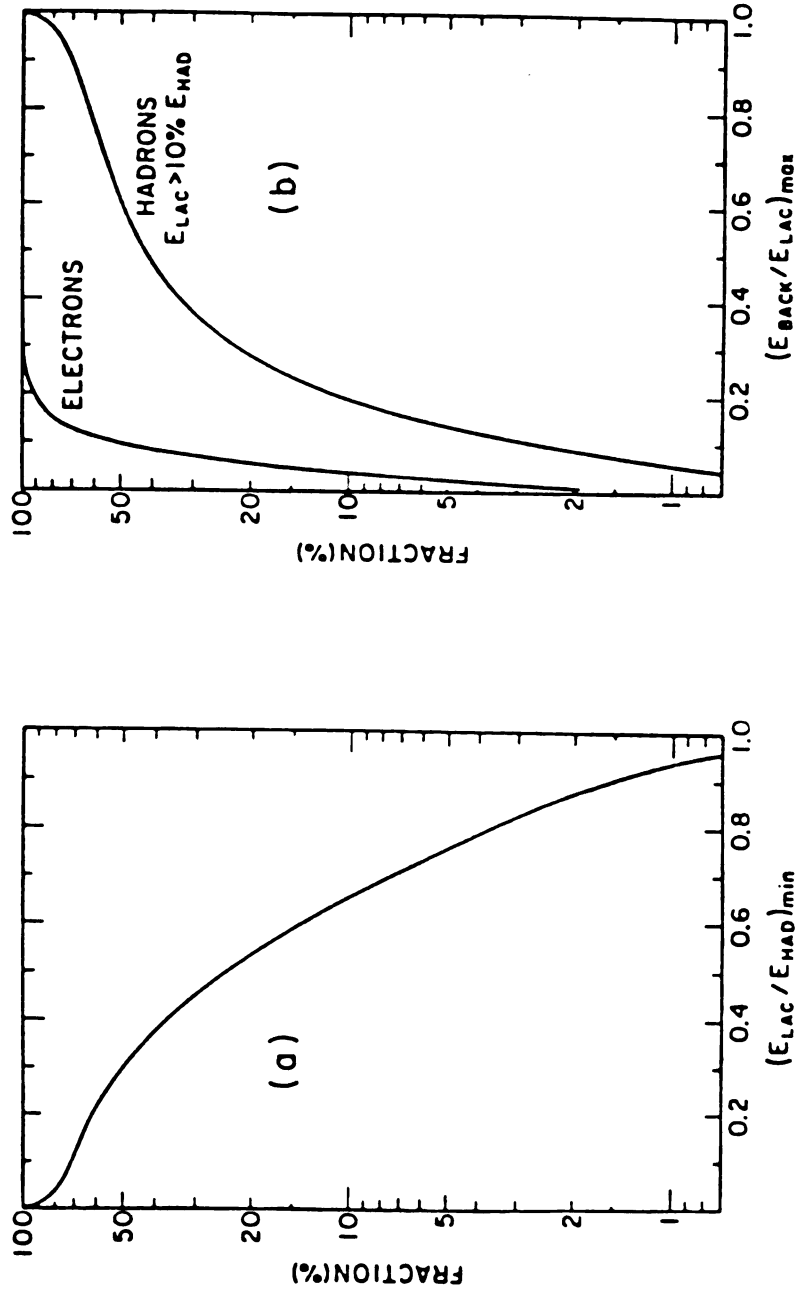
Figure 3.10; a) Fraction of hadron energy deposited b) fraction of deposited energy that is deposited in the back.

3.3 The p_T Trigger Performance and Parameterization

As described in Section 2.1.3 a large p_T signal in the LAC was required for a trigger. In this section the efficiency of the trigger is measured and then parameterized in a model based on the LAC design.

3.3.1 Trigger Efficiency

The dual trigger described in Section 2.1.3 was used to measure the trigger efficiency as a function of p_T. The electronic trigger thresholds were set at 110 mV and 150 mV, where 150 mV was used for the majority of data in the experiment. In the dual trigger mode the status of the 150 mV trigger was latched for each 110 mV trigger accepted. A data sample was used in which the criteria described in Sections 3.2.1-3 were applied to the highest energy photon in each event.

The trigger efficiency was analyzed for events with energy depositions localized to one of four x-regions; approximately equal numbers of events were localized in each region. The efficiency of the 150 mV trigger in each region is shown in Figure 3.11 where the fraction of events taken with the 110 mV threshold which would also have satisfied the 150 mV threshold is plotted with respect to

$p_{Tx} = \sum_i E_i \cdot \sin\theta_i$, where p_{Tx} is the x component of momentum in the front

49
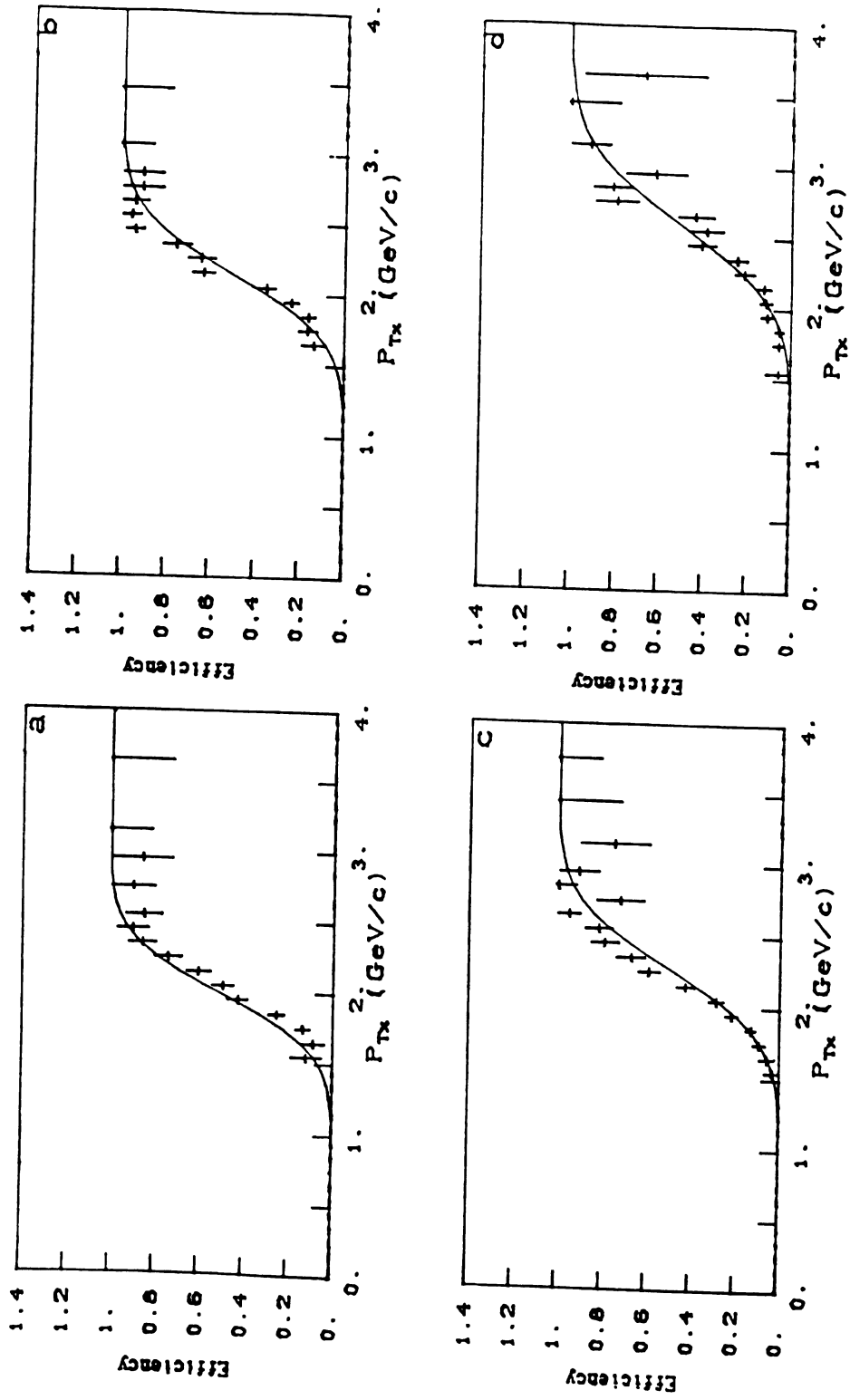
Figure 3.11; Trigger efficiency vs X(front) momentum for strips a)
2-47 b) 48-71 c) 72-89 d) 90-111.

half of the detector. The slow trigger "turn-on" in each of the four regions can be attributed to p_{Tx} "smearing" due to detector resolution, electronic noise and to variations from $\sin\theta$ weighting within each region (see Appendix A). Assuming a gaussian noise source in addition to a sharp trigger threshold in p_{Tx} the trigger turn-on can be parameterized as (see Appendix B):

$$\text{Efficiency}(p_{Tx}) = .5[1. - \text{erf}(p_{Tx}-\text{threshold},\sigma)].$$

Fitting the above function to the data in Figures 3.11 yields 2.04, 2.13, 2.22 and 2.62 ± 0.05 GeV/c for the p_{Tx} thresholds in the four regions respectively with σ's of .393, .286, .346 and .483.

3.3.2 The Trigger Model

The p_{Tx} trigger for the experiment was implemented by forming a weighted sum of the fast signal output of the x read-out strips as described in Section 2.1.3.

Nominally, a p_{Tx} signal could be formed with weights $w_i = \sin\theta_i$ where, θ_i is the laboratory polar angle of the ith strip. However, capacitive effects necessitated a departure from $\sin\theta$ weighting (see Appendix A). Image charge appears on all strips for each electromagnetic shower detected. The total amount of image charge is proportional to the ratio of detector capacitance to ballast capacitance. This ratio was kept as low as cost would allow (approximately 1/3) to minimize the image charge effects. The electronic strip weights w_i are given in Table 3.2 were chosen to

Table 3.2; Weights of the X_{front} read-outs of the Liquid Argon Calorimeter.

Range	Strip Weights					
1-6	0.000	0.304	0.302	0.300	0.298	0.297
7-12	0.295	0.293	0.291	0.289	0.288	0.286
13-18	0.285	0.283	0.281	0.279	0.277	0.275
19-24	0.273	0.272	0.270	0.268	0.266	0.264
25-30	0.262	0.260	0.259	0.257	0.255	0.253
31-36	0.251	0.249	0.247	0.245	0.244	0.242
37-42	0.240	0.238	0.236	0.234	0.232	0.230
43-48	0.228	0.227	0.225	0.223	0.221	0.219
49-54	0.217	0.215	0.213	0.211	0.210	0.208
55-60	0.206	0.204	0.202	0.200	0.198	0.196
61-66	0.194	0.192	0.191	0.189	0.187	0.185
67-72	0.183	0.181	0.179	0.177	0.175	0.173
73-78	0.171	0.170	0.168	0.166	0.164	0.162
79-84	0.160	0.158	0.156	0.154	0.153	0.151
85-90	0.149	0.147	0.145	0.143	0.141	0.139
91-96	0.137	0.135	0.133	0.131	0.130	0.128
97-102	0.126	0.124	0.121	0.120	0.118	0.116
103-108	0.114	0.112	0.110	0.109	0.107	0.105
109-112	0.103	0.101	0.099	0.000		

compensate for the expected capacitive effects and roughly correspond to $\sin\theta_i$. A simple model of the effects of the trigger electronics is given by

$$T = A\Sigma E_i [w_i - \alpha] ,$$

where E_i is the energy deposited in the front half of the detector in strip(i), α is an image charge coefficient and A is a scale factor (see Appendix A).

In events where energy depositions are confined to a localized region of the detector the strip weights w_i are slowly varying and result in a approximately constant p_{Tx} threshold throughout the region. The trigger-model parameters, α,A in addition to a gaussian noise parameter σ were selected to best reproduce the thresholds in p_{Tx} described in the previous section.

A vertical (y) dependence to the trigger threshold was not anticipated. However, it was observed that the π^o yield, as shown in Figure 3.12, was not symmetric above and below the beam line. After careful study, the only reasonable source of this effect was a vertical asymmetry in the trigger.

The detector was divided into four vertical regions of equal width. Thresholds were determined for the four regions by the method described in the previous section; the trigger variable T was used instead of p_{Tx}. These thresholds in T are shown as a function of y (LAC) in Figure 3.13. A small but linear decrease in the threshold with
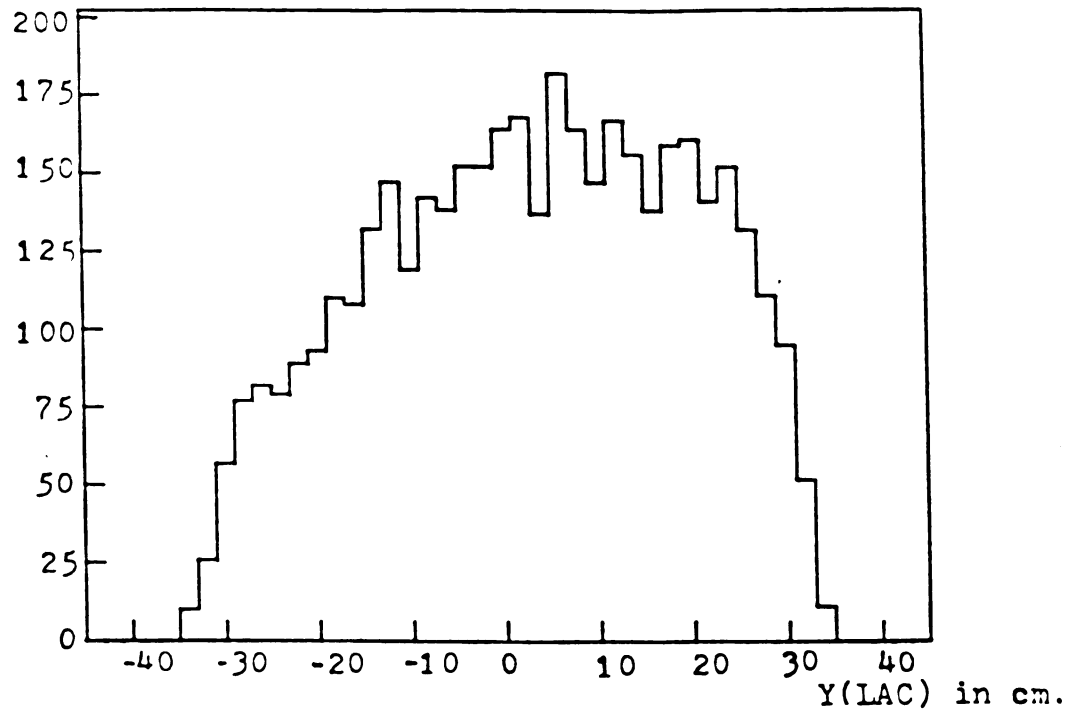
Figure 3.12; π^0 distribution in Y(LAC).
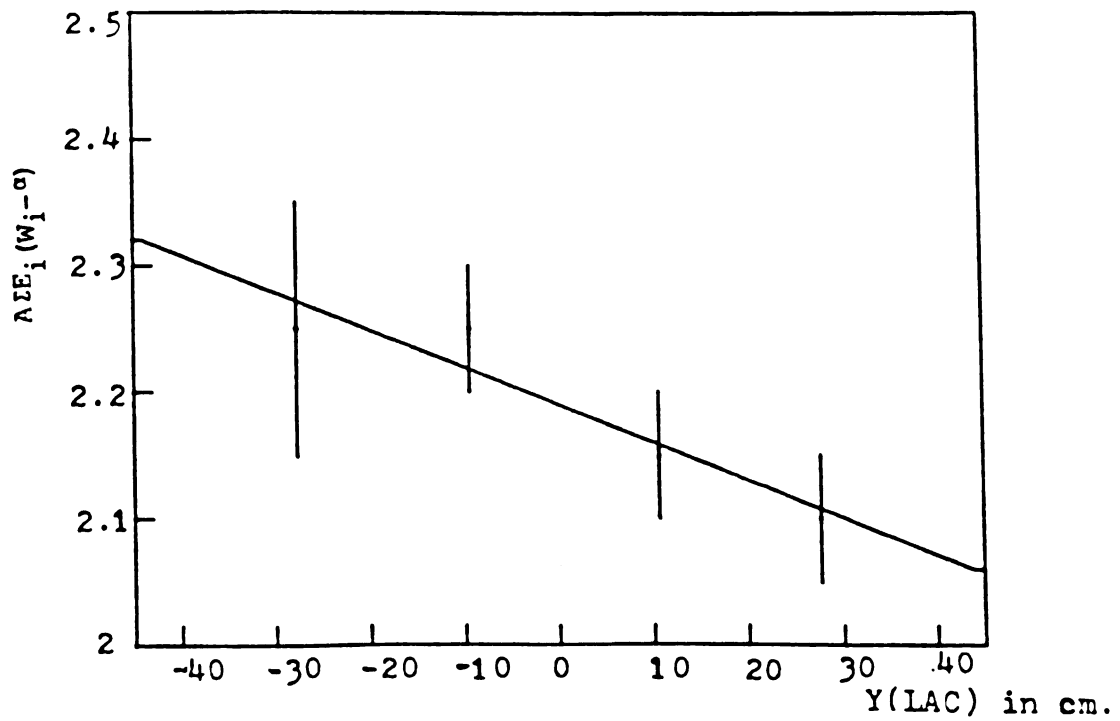
Figure 3.13; Trigger variable value at threshold.

increasing y (LAC) is observed. A linear fit to this data was incorporated into the parameterization as follows:

$$T = A\sum_i E_i (w_i - \alpha)/(ay_i + b)$$

The parameters A and α were then slightly adjusted to maintain the p_{Tx} dependence shown in Figures 3.11. The final values for the trigger-model parameters were:

A=1.0, α=0.067, a=-1.35x10^{-3}, b=1.0, σ=.3 and trigger threshold=2.05 (see Appendix B).

One explanation of this effect requires that small changes occur in the fast signal pulse shape depending upon the vertical position of the shower. The integrated pulse shows no such effect as the energy calibration (and thus the π^0 mass) is found to be invariant with vertical position of photon showers. Referring again to Figure 3.11, Monte Carlo generated events, when required to pass the trigger-model, reproduce the threshold behavior across the detector as shown by the curves which overlay the data.

3.3.3 Front/Back Energy Partition

The trigger used only the energy depositions in the first 12.5 radiation lengths of the detector. In order to simulate the trigger for Monte Carlo generated photons, a model for the energy split between back and front was required. The $E_{(back)}/E_{(total)}$ distributions in four energy ranges are shown in Figures 3.14. The most probable value of $E_{(back)}/E_{(total)}$ grows linearly with increasing photon energy,
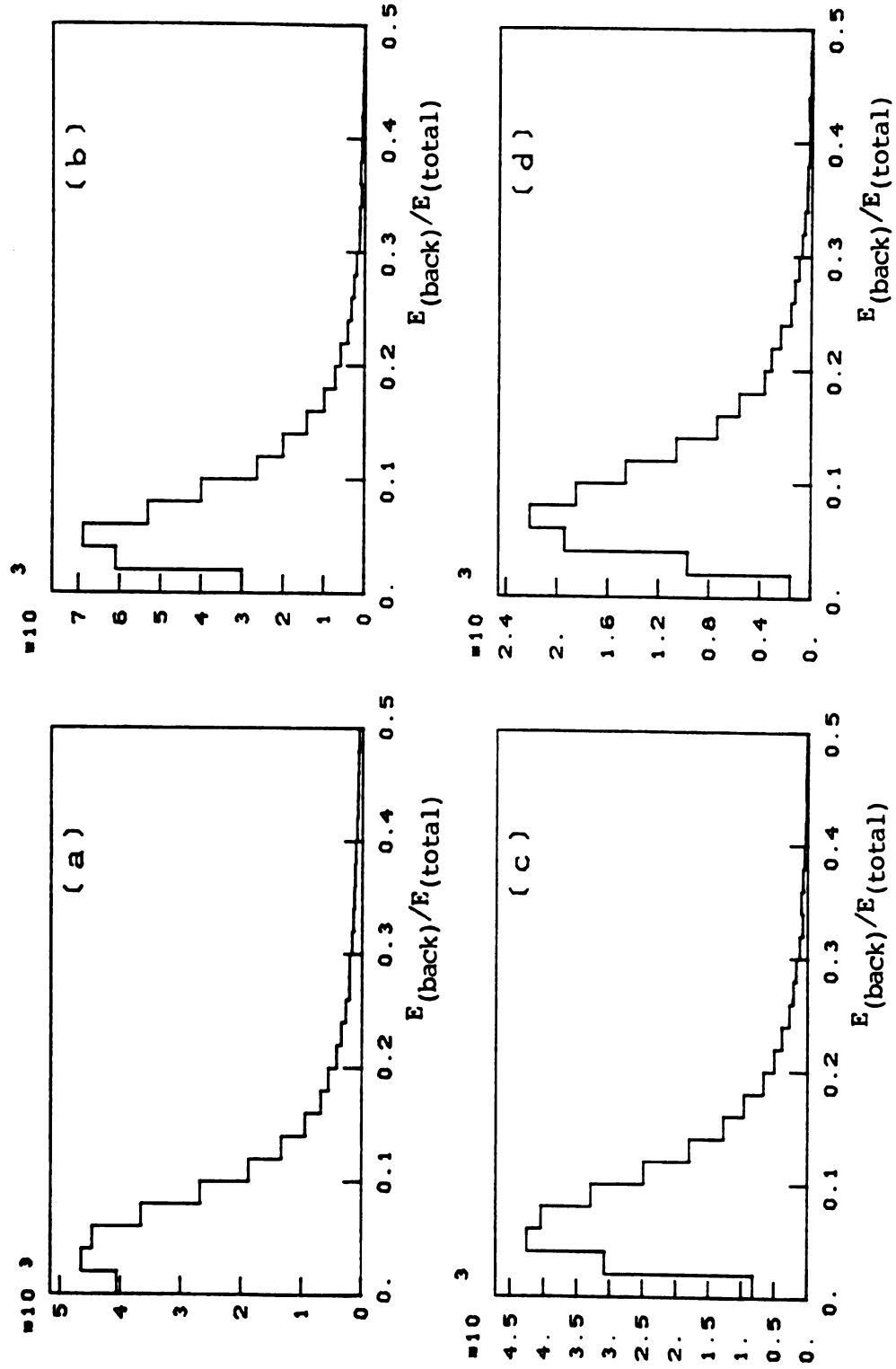
Figure 3.14; Back to total energy ratios for a) 0-5 GeV, b) 5-10 GeV c) 10-15 GeV d) 15-20 GeV photons.

however the tails in these distributions could not easily be parameterized. Therefore, the $E_{(back)}/E_{(total)}$ ratio for each generated photon was selected randomly from these distributions in the Monte Carlo program.

Chapter 4

Direct-Photon, π^0 and η Cross Section Determination

This chapter presents the steps in the analysis leading to a determination of the direct-photon, π^0 and η invariant cross sections.

4.1 Single-Photon, π^0 and η Selection Criteria

In addition to the time, direction and hadron cuts described in Sections 3.2.1-3.2.3, a minimum energy of 1 Gev was required for each photon identified in the reconstruction program. This eliminated backgrounds due to fluctuations in the tails of electromagnetic showers and electronic noise. To eliminate photons with energy losses near the edges of the detector all reconstructed photons were required to be at least 5 cm from each edge.

The two photon effective mass spectra for all photon multiplicities of 8 or less with $p_T \geq 2.5$ GeV/c is shown in Figure 4.1. Six regions within the mass spectrum were selected; the π^0 and η mass regions with 25 and 50 MeV width respectively, and the π^0 and η sidebands with 80
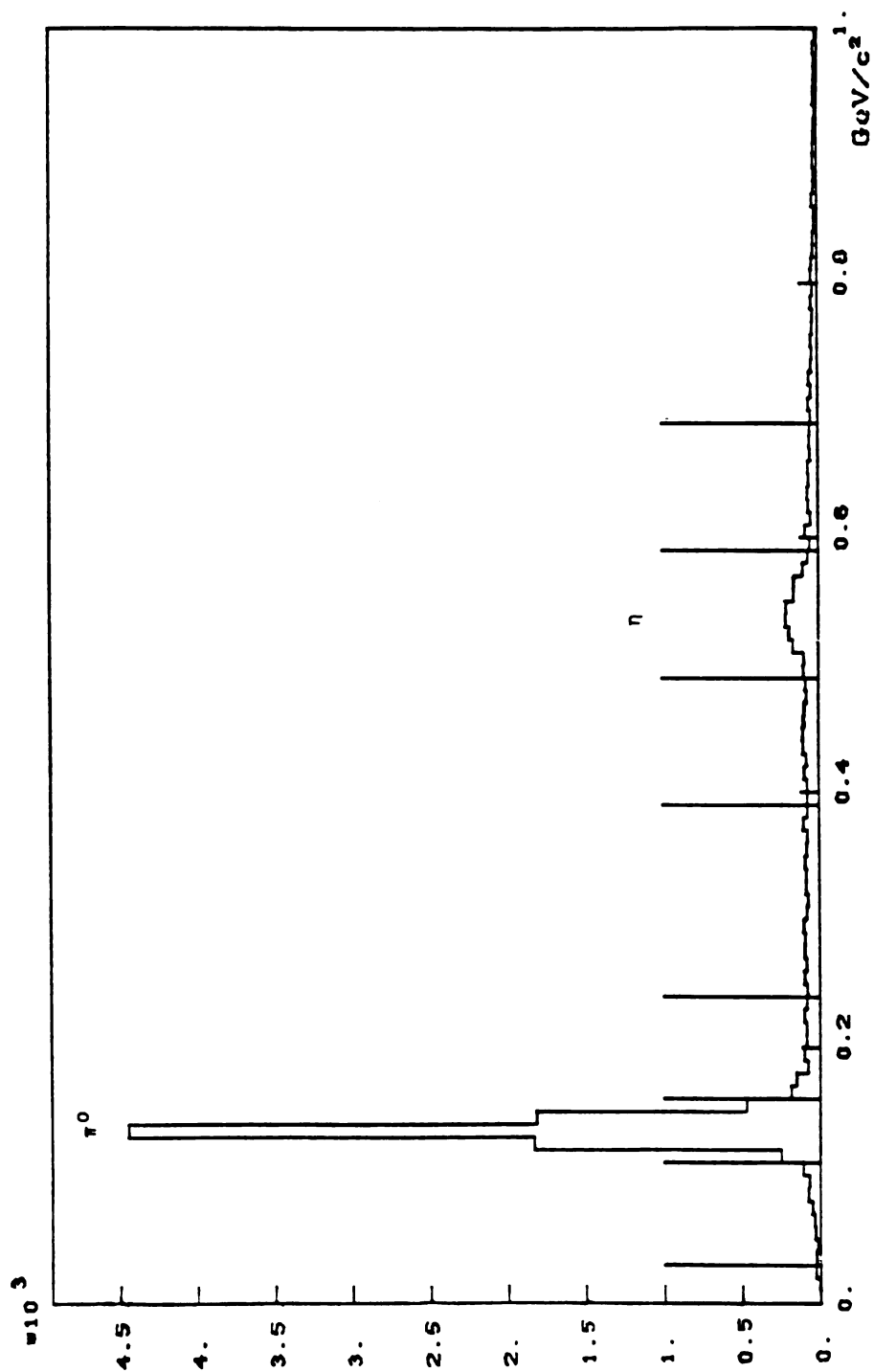
Figure 4.1; 2 Photon mass spectrum for all photon multiplicities ≤ 8 with $P_T > 2.5$ GeV/c and asymmetry $< .8$ in the π^0 and η mass range. Peak and sideband regions are delineated by vertical lines.

and 100 MeV widths respectively. The boundaries of the six regions are marked by vertical lines on the plot.

A photon pairing with an effective mass within either peak region was designated as as a π^0 or η meson decay. A photon not included in any π^0 and η pairing was designated as a single photon. A photon pairing with an effective mass falling within a sideband region was designated as a sideband π^0 or η.

4.2 π^0 and η Invariant Cross Sections

The π^0 and η invariant cross section determination consisted of weighting the data for detector acceptance, subtracting background and normalizing to the target and beam parameters.

4.2.1 Subtraction of π^0 and η Background

In events with only two observed photons, the background to the π^0 and η production is composed of photons from two separate meson decays where the second photon from each decay misses the detector or is below the minimum energy criteria. In events with more than two observed photons, a combinatorial component in the background due to ambiguities in photon pairing is also present.

Two photon effective mass spectra for various ranges in p_T for two-photon events were shown previously in Figure 3.4a and for three photon events in Figure 3.4b. The sidebands in the two photon event spectra are less populated in comparison to the peak than is the case in the three photon event spectra where the expected combinatorial ambiguities in photon pairing are present. An estimate of the background can be made in each case by extrapolating the sideband population under the peak.

To minimize effects from observed differences in the mass spectra profiles with respect to changes in p_T, photon multiplicity and meson decay asymmetry (see Appendix C for the definition of decay asymmetry), the effective mass data were separated in these variables. Mass plots were generated for combinations of photon multiplicity, selected ranges in p_T and asymmetry.

As an example of the quality of the background fitting procedure, the π^0 and η plots for a photon multiplicity of two, a p_T range of 2.0-2.5 GeV/c and a asymmetry range of 0.0-0.3 are shown in Figure 4.2. The mass spectra in the mass and sideband regions are fit to a polynomial background plus a gaussian mass peak. After subtracting the polynomial background from the mass spectra, the gaussian peaks shown in Figures 4.2c-d are obtained. Comparable mass plots for a photon multiplicity of three, a p_T range of 2.5-3.0 GeV/c, and a asymmetry range of .6-.8 are shown in Figure 4.3. Similar fits were made to all the generated mass plots.
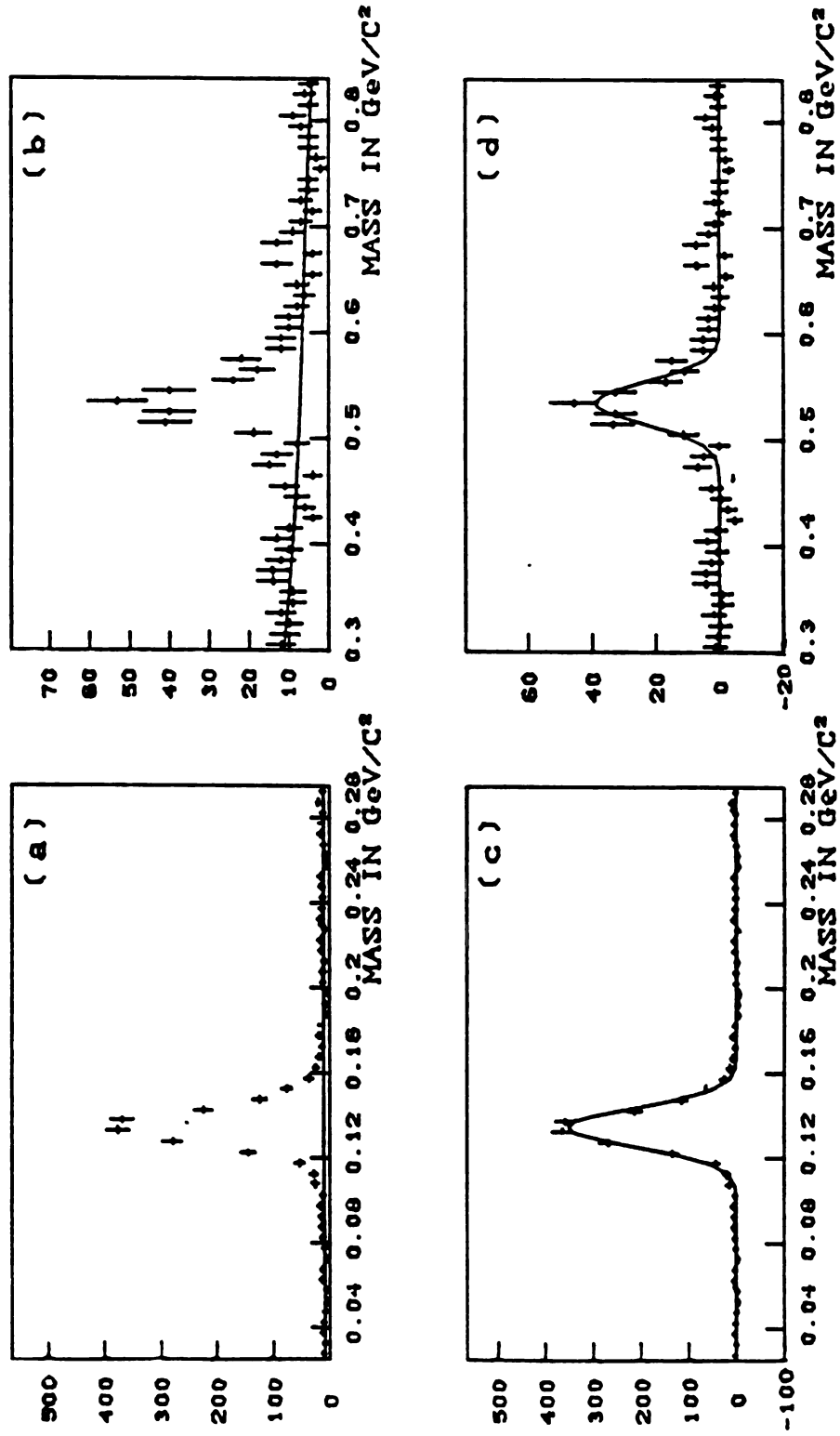
Figure 4.2; 2γ mass spectra for p_T 2.0-2.5 GeV/c, asymmetry .0-.3 and photon multiplicity 2, a) π^0 mass region b) η mass region c) π^0 background subtracted d) η background subtracted.
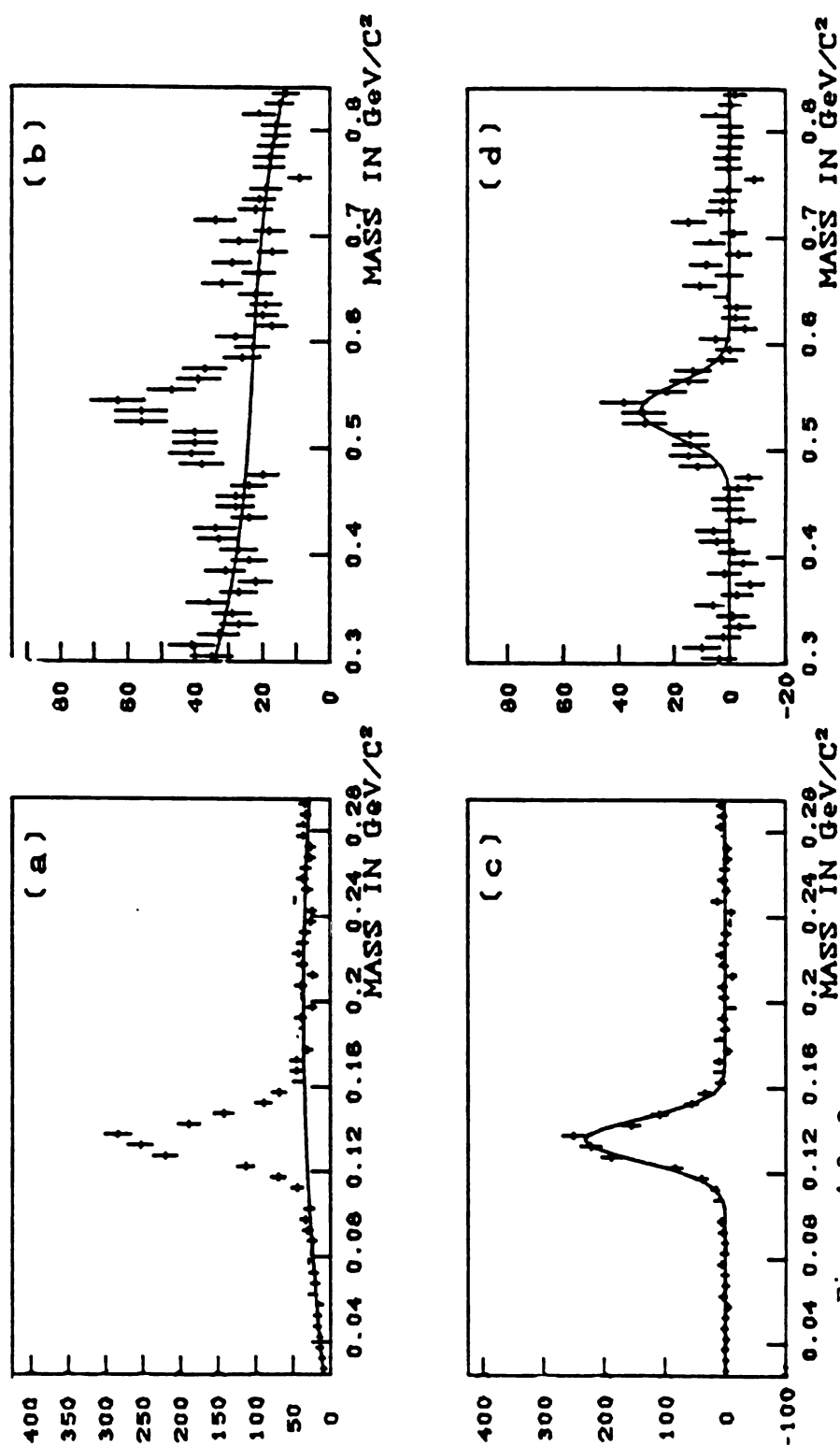
Figure 4.3: 2γ mass spectra for p_T 2.5-3.0 GeV/c, asymmetry .6-.8 and photon multiplicity 3, a) π^0 mass region b) η mass region c) π^0 background subtracted d) η background subtracted.

The background estimates were made by normalizing the sideband data to the background under the peaks. The normalization factors were obtained for the various combinations of photon multiplicity, P_T and asymmetry by determining the integrals of the background fits in the meson mass regions and then dividing the integrals by the sum of the data in the sideband regions.

4.2.2 Determination of the Acceptance of the Detector

An analysis of the decay asymmetry distributions confirms the effectiveness of the background subtraction procedure. The asymmetry distributions for the data in the π^0 and η mass regions are shown in Figures 4.4a-b with the asymmetry distributions for the background as determined from the weighted sideband data shown as dashed profiles overlying the plots. The data after background subtraction are shown in Figures 4.4c-d. The background subtracted distributions fall with increasing asymmetry where the opening angles of the meson decays are larger. The η distributions show a poorer acceptance than the π^0's due to the greater mass of the η and correspondingly greater decay angles. In the determination of cross sections a upper limit of .8 in asymmetry was applied to the data to avoid the poor geometric acceptance and strong backgrounds at high asymmetry.

A Monte Carlo procedure was used to determine the geometric and trigger acceptances. For each π^0 or η (peak and sideband) in the data
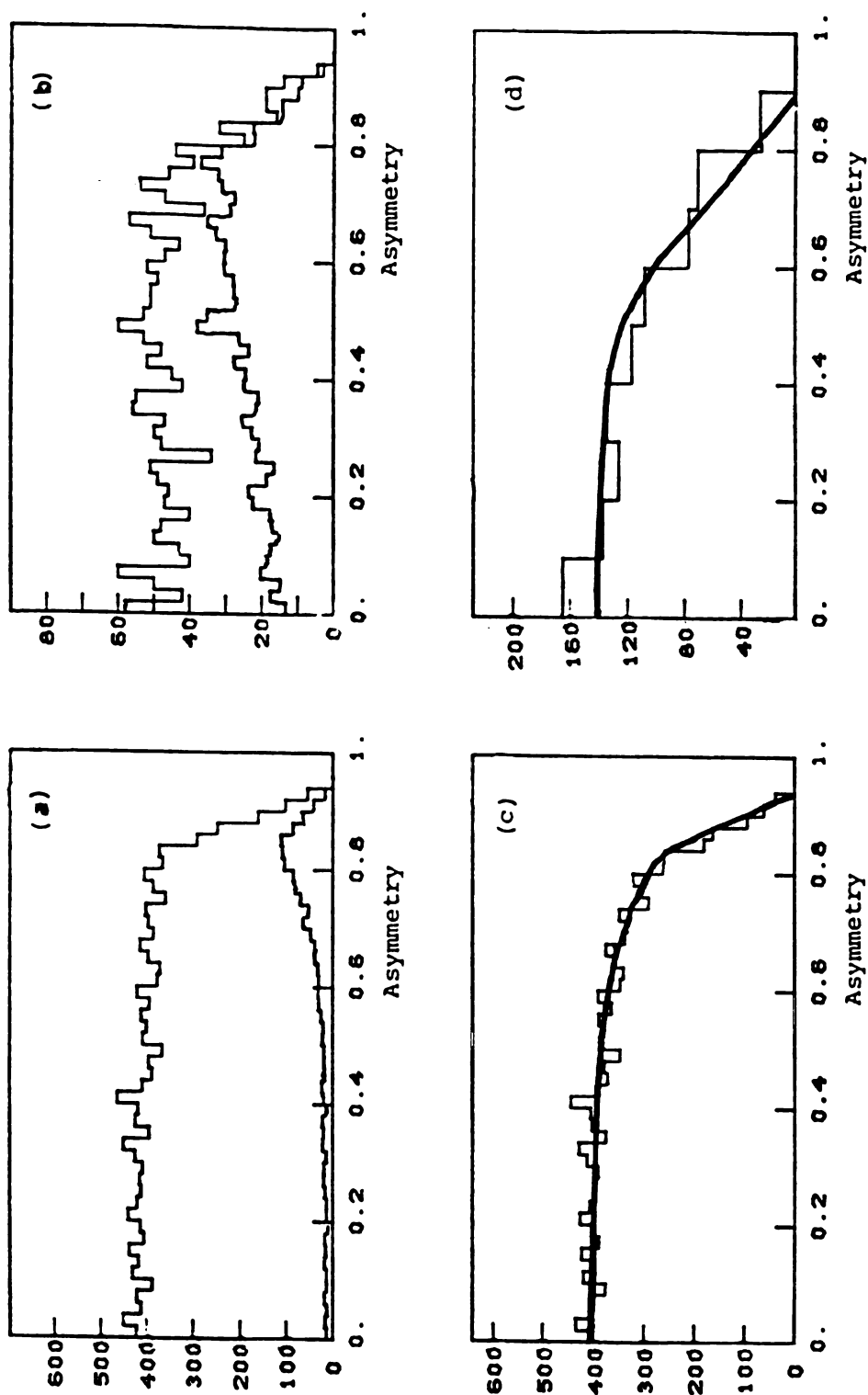
Figure 4.4; Asymmetry distributions for a) π^0 mass region and b) η mass region, where the sideband distributions are shown as dashed histograms. Background subtracted asymmetry distributions and Monte Carlo predictions (curves) for c) π^0 mass region and d) η mass region.

a set of two-photon decays was generated with the same 3-momentum. The decay photons were then tested for geometric acceptance within the fiducial region. Both generated photons in each decay were also required to be above 1 GeV in energy. The trigger parameterization described in Section 3.3.2 along with the back to total energy partitioning procedure described in Section 3.3.3 were then jointly applied to each decay meeting the above criteria to obtain the trigger efficiency. Particular care was taken to include the effects of any additional energy (photons and hadrons) which accompanied the meson decay. Decays were generated until ten were accepted or a maximum of 100 decays was reached. The ratio of accepted to generated decays defined the geometric acceptance while the trigger efficiency was defined as the average of the trigger efficiencies for the accepted decays.

In a Monte Carlo study discussed elsewhere[31] the reconstruction efficiencies for π^0 and η were determined for various ranges of asymmetry at photon multiplicities of 2 to 8 and are given in Table 4.1.

4.2.3 Fiducial Limits in Rapidity and Vertical Position

The p_T trigger threshold as described in Section 3.3.1 decreased smoothly from the beam side to the away side of the detector. Near the edges of the detector the geometric efficiency for accepting both

Table 4.1; Software reconstruction efficiencies of the π^0 and η with respect to asymmetry and multiplicity.

Decay Asymmetry	Photon Multiplicity						
	2 γ	3 γ	4 γ	5 γ	6 γ	7 γ	8 γ
.0 to .1	.993	.946	.898	.890	.863	.863	.863
.1 to .2	.993	.946	.898	.890	.863	.863	.863
.2 to .3	.993	.946	.898	.890	.863	.863	.863
.3 to .4	.993	.946	.898	.890	.863	.863	.863
.4 to .5	.993	.946	.898	.890	.863	.863	.863
.5 to .6	.993	.946	.898	.890	.863	.863	.863
.6 to .7	.993	.946	.868	.818	.748	.748	.748
.7 to .8	.975	.877	.837	.748	.663	.663	.663

photons from a π^0 or η was lower than for the center of the detector. Additionally, for fixed p_T the energy is higher at high rapidity than at low rapidity, resulting in smaller opening angles and better geometric acceptance on the beam side of the detector (See Appendix C).

Fiducial limits in vertical position and rapidity were selected to exclude regions of the detector where the combined trigger and geometric efficiency was less than 10%. Table 4.2 gives the rapidity and vertical position limits of ranges in p_T for the π^0 and η.

4.2.4 Inclusive π^0 and η Production

Each event in the π^0, η or $\pi^0(\eta)$ sidebands that fell within the rapidity and position limits given in Table 4.2 was weighted by the inverse of the trigger (ϵ_t), geometric (ϵ_g) and reconstruction (ϵ_r) efficiencies described in the previous section. Additionally, the azimuthal range $(\Delta\Phi)$ of the detector as determined from the vertical position limits in Table 4.2, and applied as a correction for azimuthal acceptance. The combined correction for detector acceptance is summarized as follows:

$$\text{Correction} = 1/(\epsilon_t)(\epsilon_g)(\epsilon_r)(\Delta\Phi/2\pi)$$

This factor was multiplied by a background weight, as described in Section 4.2.1, normalizing the sidebands to a background estimate. The inclusive production for each range of p_T and rapidity was then obtained by subtracting the corrected $\pi^0(\eta)$ sideband data from the

Table 4.2; Fiducial limits in rapidity and vertical position in the LAC.

P_T (GeV/c)	π^0		η	
	Rapidity	Vertical Position (cm)	Rapidity	Vertical Position (cm)
2.0 to 2.1	2.25 to 2.75	-26.00 to 28.00		
2.1 to 2.3	2.25 to 2.90	-26.00 to 28.00	2.50 to 2.90	-16.00 to 21.00
2.3 to 2.5	2.20 to 3.05	-26.00 to 26.00	2.40 to 3.00	-16.00 to 21.00
2.5 to 2.7	2.20 to 3.05	-33.00 to 33.00	2.40 to 3.15	-24.00 to 21.00
> 2.7	2.20 to 3.20	-33.00 to 33.00	2.40 to 3.20	-24.00 to 21.00

corrected π^0 and η data. The inclusive production of π^0 and η for incident π^+ and p are given in Table 4.3.

4.2.5 Corrections to Beam

As described in Section 2.2.1 the fraction of each beam spill during which the experiment was unable to accept events (dead time) was monitored. The total beam was monitored as well. By applying corrections for dead time and some smaller corrections to be described, the total number of beam particles which struck the targets while the experiment was able to accept events was determined.

In passing through a target a beam is attenuated by absorption. The total number of beam particles $N(z)$ seen at a distance z within the target is N, the initial number of beam particles multiplied by the factor $\exp(-z/\lambda)$ where $\lambda=49.9$ cm is the absorption length (in this case for carbon). The carbon targets presented a total of 2.54 cm depth of target to the beam. By integrating $N(z)$ over the target depth and dividing the result by the total target depth a average $N(z)$ is determined. For the two carbon targets together a attenuation factor of .975 is applied to the total number of beam particles to get the effective average number of beam particles seen in the targets.

The incident beam consisted of protons, positive pions (about 13%), K^+ and from previous beam studies μ^+ (approximately 1%). At the start

Table 4.3: Inclusive π^0 and η event yields for incident p and π^+.

p_T (GeV/c)	$pC \to \pi^0 + X$	p_T (GeV/c)	$\pi^+C \to \pi^0 + X$	p_T (GeV/c)	$pC \to \eta + X$	p_T (GeV/c)	$\pi^+C \to \eta + X$
2.0 to 2.1	$(1.07 \pm 0.03) \times 10^6$	2.0 to 2.1	$(1.17 \pm 0.09) \times 10^5$	2.1 to 2.2	$(1.04 \pm 0.20) \times 10^5$	2.1 to 2.3	$(2.56 \pm .89) \times 10^4$
2.1 to 2.2	$(9.01 \pm 0.24) \times 10^5$	2.1 to 2.2	$(1.15 \pm 0.08) \times 10^5$	2.2 to 2.3	$(7.23 \pm 1.46) \times 10^4$	2.3 to 2.5	$(2.68 \pm .61) \times 10^4$
2.2 to 2.3	$(7.19 \pm 0.10) \times 10^5$	2.2 to 2.3	$(8.52 \pm 0.63) \times 10^4$	2.3 to 2.5	$(1.47 \pm 0.17) \times 10^5$	2.5 to 2.7	$(1.02 \pm .32) \times 10^4$
2.3 to 2.5	$(1.12 \pm 0.02) \times 10^6$	2.3 to 2.5	$(1.36 \pm 0.07) \times 10^5$	2.5 to 2.7	$(9.62 \pm 0.99) \times 10^4$	2.7 to 3.2	$(1.24 \pm .27) \times 10^4$
2.5 to 2.7	$(5.43 \pm 0.16) \times 10^5$	2.5 to 2.7	$(8.12 \pm 0.49) \times 10^4$	2.7 to 3.0	$(6.28 \pm 0.70) \times 10^4$	3.2 to 4.0	$(1.26 \pm .80) \times 10^3$
2.7 to 3.0	$(3.90 \pm 0.10) \times 10^5$	2.7 to 3.0	$(6.05 \pm 0.38) \times 10^4$	3.0 to 3.4	$(2.84 \pm 0.32) \times 10^4$	4.0 to 5.0	$(2.70 \pm .20) \times 10^2$
3.0 to 3.3	$(1.38 \pm 0.05) \times 10^5$	3.0 to 3.3	$(2.24 \pm 0.20) \times 10^4$	3.4 to 4.0	$(8.55 \pm 1.71) \times 10^3$		
3.3 to 3.6	$(4.64 \pm 0.29) \times 10^4$	3.3 to 3.6	$(7.47 \pm 1.02) \times 10^3$	4.0 to 5.0	$(1.03 \pm 0.48) \times 10^3$		
3.6 to 4.0	$(1.82 \pm 0.17) \times 10^4$	3.6 to 4.0	$(1.98 \pm 0.53) \times 10^3$				
4.0 to 4.5	$(5.54 \pm 0.87) \times 10^3$	4.0 to 4.5	$(7.86 \pm 2.91) \times 10^2$				
4.5 to 5.0	$(7.06 \pm 3.44) \times 10^2$						

of the experiment the helium pressure in the beam Cerenkov counter mentioned in Section 2.1.1 was adjusted to maximize the π^+ detection efficiency.

From inspection of the pressure curve it was determined that 2% of the particles tagged as π^+ were protons. The overall efficiency of the detector was found to be 80%. The total number of incident particles tagged as π^+ or proton were then accordingly adjusted for contamination and counter inefficiency. Correction was also made for the 1% μ^+ contamination. The 3% K^+ component in the beam was identified by the Cherenkov as π^+ and due to the expected dominance of the u quark in direct photon production (see Section 1.4) no correction for K^+ contamination to the π^+ signal was made.

The 50 MHz radio-frequency of the Fermilab accelerator resulted in a 19 ns bucket structure as observed in Figure 3.9. The 10^7 particle per second beam spill intensity resulted in an average beam bucket occupancy of 0.2. By assuming a Poisson distribution for the bucket occupancy the probability for a empty bucket was 81.87%, for a singly occupied bucket 16.37% and for a doubly occupied bucket 1.64%. Higher occupancies have probabilities on the order of 0.01% or less. As described in Sections 2.2.1 and 2.2.3 the trigger vetoed events with multiple particle hits in both planes of the beam hodoscope. From geometric considerations the probability for a two particle event to overlap in one or both planes of the beam hodoscope and thereby remain unvetoed was determined to be 21.7%. As a result 21.7% of the .0164/.1637 fraction of events with two particles passed the trigger

and contributed to the total beam particle count of the experiment. The correction is then the product of the above (2.1%). Additionally, it was determined in off-line analysis that due to discriminator problems .5% of all triggered events had two particle hits in both planes of the beam hodoscope. Rescaling for the extra particles from the two particle events that triggered results in a 2.1% plus .5% correction which is applied as a scale factor of 1.026 to the total number of beam particles.

Data was taken without targets to measure backgrounds from interactions in non-target material in the target area. The results for π^0 and η were consistent with the target data but lacked sufficient statistics to adequately determine a p_T dependent background subtraction. Instead the total particle count was scaled up by a factor of 1.03 which gives the same effect as a background subtraction with the same p_T dependence as that of the target data.

The combined effect of these corrections was to increase the total beam particle count by a 3% for incident proton beam and decrease the particle count for incident π^+ beam by 5%.

4.2.6 π^0 and η Invariant Cross Section Calculations and Results

In preliminary results of the π^0 and η cross sections it was determined that within statistical uncertainty there was no dependence in rapidity range observed. Therefore, in order to maximize the data the full range of rapidity for each p_T range listed in Table 4.2 was used in the final calculations. By using the corrections described in the preceding section to get the total beam particle count and applying a formula for the cross section described in Appendix D to the data in Table 4.3 the results for the π^0 and η invariant cross sections for both incident π^+ and p are obtained and given in Table 4.4. The listed errors are statistical. However, a systematic error due mainly to the calibration of the energy scale to the π^0 mass is also present. This calibration resulted in a 1.8% shift in the η mass from its accepted value. A shift in the energy scale of the experiment of this magnitude would result in an uncertainty in the cross sections of up to 16%. Therefore a ± 16% systematic error should be assigned to each cross section reported here.

For use in single photon background studies a function of the form $\exp(\alpha + \beta p_T)$ was fit to the π^0 and η invariant cross sections determined from the incident proton data. Values of $\alpha = -57.9 \pm 0.06$ and $\beta = -3.97 \pm 0.03$ $(\text{GeV/c})^{-1}$ were obtained for the π^0 data with $\alpha = -59.2 \pm 0.33$ and $\beta = -3.71 \pm 0.12$ $(\text{GeV/c})^{-1}$ obtained for the η data.

Table 4.4; π^0 and η invariant cross sections for incident p and π^+ at 200 GeV/c with a carbon target in the center of mass rapidity interval (-0.80 to 0.20).

$Ed\sigma/d^3p\,(cm^2/GeV^2)/nucleus$

P_T (GeV/c)	$pC \to \pi^0 + X$	P_T (GeV/c)	$\pi^+ C \to \eta + X$	P_T (GeV/c)	$pC \to \eta + X$	P_T (GeV/c)	$\pi^+ C \to \pi^0 + X$
2.0 to 2.1	$(2.15\pm0.06)\times10^{-29}$	2.0 to 2.1	$(1.43\pm0.14)\times10^{-29}$	2.1 to 2.2	$(6.38\pm1.29)\times10^{-30}$	2.1 to 2.3	$(5.08\pm2.15)\times10^{-30}$
2.1 to 2.2	$(1.46\pm0.04)\times10^{-29}$	2.1 to 2.2	$(1.07\pm0.09)\times10^{-29}$	2.2 to 2.3	$(4.23\pm0.90)\times10^{-30}$	2.3 to 2.5	$(3.37\pm0.88)\times10^{-30}$
2.2 to 2.3	$(1.02\pm0.03)\times10^{-29}$	2.2 to 2.3	$(7.59\pm0.70)\times10^{-30}$	2.3 to 2.5	$(2.68\pm0.33)\times10^{-30}$	2.5 to 2.7	$(8.43\pm3.40)\times10^{-31}$
2.3 to 2.5	$(5.72\pm0.11)\times10^{-30}$	2.3 to 2.5	$(4.38\pm0.29)\times10^{-30}$	2.5 to 2.7	$(1.31\pm0.14)\times10^{-30}$	2.7 to 3.2	$(3.77\pm0.97)\times10^{-31}$
2.5 to 2.7	$(2.53\pm0.08)\times10^{-30}$	2.5 to 2.7	$(2.52\pm0.18)\times10^{-30}$	2.7 to 3.0	$(4.86\pm0.57)\times10^{-31}$	3.2 to 4.0	$(1.75\pm1.53)\times10^{-32}$
2.7 to 3.0	$(9.44\pm0.24)\times10^{-31}$	2.7 to 3.0	$(9.79\pm0.73)\times10^{-31}$	3.0 to 3.4	$(1.49\pm0.18)\times10^{-31}$	4.0 to 5.0	$(3.12\pm2.51)\times10^{-33}$
3.0 to 3.3	$(3.01\pm0.12)\times10^{-31}$	3.0 to 3.3	$(3.30\pm0.35)\times10^{-31}$	3.4 to 4.0	$(2.67\pm0.54)\times10^{-32}$		
3.3 to 3.6	$(9.25\pm0.60)\times10^{-32}$	3.3 to 3.6	$(1.01\pm0.16)\times10^{-31}$	4.0 to 5.0	$(1.51\pm0.77)\times10^{-33}$		
3.6 to 4.0	$(2.52\pm0.25)\times10^{-32}$	3.6 to 4.0	$(1.67\pm0.57)\times10^{-32}$				
4.0 to 4.5	$(5.47\pm0.89)\times10^{-33}$	4.0 to 4.5	$(4.94\pm2.24)\times10^{-33}$				
4.5 to 5.0	$(6.28\pm3.19)\times10^{-34}$	4.5 to 5.0	$(6.72\pm7.92)\times10^{-34}$				
		5.0 to 6.0	$(1.10\pm0.63)\times10^{-33}$				

4.3 Direct-Photon and π^0 Invariant Cross Sections and their Ratio

The invariant cross section was determined for direct-photons by first finding the direct-photon to π^0 ratio. The π^0 invariant cross sections listed in Table 4.4 were then used to recover the direct-photon invariant cross section.

4.3.1 Single Photon Signal

Each photon designated as a single photon in the procedure described in Section 4.2.1 was corrected for trigger and azimuthal acceptance, and for losses due to single photons randomly pairing with another photon to form a π^0 or η effective mass. The ranges in p_T, rapidity and vertical position for π^0s given in Table 4.2 were also used in the selection of the single photon sample. For each single photon the residual energy contribution to the trigger was determined for all other photons in the x-front view of the detector. Then in a procedure analogous to that outlined in Section 4.2.2 the back to total energy partitioning procedure of Section 3.3.3 was applied to the single photon energy a total of 10 times. For each generated back to total partition a trigger efficiency was determined. The average of the 10 efficiencies was then taken as the trigger efficiency (ϵ_t) of the single photon event. In order to compensate for single photons eliminated from under the π^0 and η peaks, a normalized number of single

photons from the π^0 and η sidebands were added to the singles spectrum. The azimuthal range ($\Delta\Phi$) of the detector for the fiducial limits at the position and p_T of each single photon was determined. Each single photon was then weighted by $1/(\epsilon_t)$ ($\Delta\Phi/2\pi$). Additionally, a downward correction for contamination due to software reconstruction inefficiencies of the π^0 and η was applied. This correction varied from 2.1% at 2.0-2.3 GeV/c p_T to 1.4% at $p_T > 3.5$ GeV/c.[31] The resulting weighted single photon distribution was then divided by the inclusive π^0 production to produce a combined inclusive single photon "γ" to π^0 ratio. This data is presented in Table 4.5 under the heading, data ("γ"/π^0). The sources of background to the direct-photon ratio in the above data will be presented in the following sections.

4.3.2 Backgrounds to the (Direct-Photon)/π^0 Signal

Photons from unreconstructed π^0, η, η', ω decays and from charged hadrons which simulated photon showers by interacting early in the detector contribute a major part of the data "γ"/π^0. To recover the direct-photon contribution these backgrounds must be eliminated.

These contributions to the background were modeled by use of Monte Carlo techniques which relied on the π^0 and η cross section results of Section 4.2.6, estimates of the η' and ω yields and evaluation of the hadron contamination.

Table 4.5; γ/π° data and backgrounds.

Incident p_T(GeV/c)	Proton Data "γ"/π°	Incident p_T(GeV/c)	π+ Data "γ"/π°	p_T(GeV/c)	π°"γ"/π°	η"γ"/π°	charged Hadron"γ"/π°	η'"γ"/π°	ω"γ"/π°	Total
2.0-2.1	.240±.012	2.0-2.1	.294±.052	2.0-2.1	.137	.041	.042	.006	.005	.231
2.1-2.2	.208±.011	2.1-2.3	.236±.029	2.1-2.2	.125	.039	.041	.006	.005	.216
2.2-2.3	.213±.011	2.3-2.6	.176±.021	2.2-2.3	.117	.038	.040	.005	.004	.204
2.3-2.4	.177±.010	2.6-3.0	.151±.021	2.3-2.4	.111	.037	.039	.005	.004	.196
2.4-2.5	.164±.011	3.0-3.5	.157±.032	2.4-2.5	.106	.036	.039	.005	.004	.190
2.5-2.7	.188±.010	3.5-4.0	.394±.189	2.5-2.7	.099	.035	.038	.004	.004	.180
2.7-3.0	.180±.010	4.0-5.0	.421±.286	2.7-3.0	.090	.033	.036	.004	.003	.166
3.0-3.5	.184±.013	5.0-6.0	.583±.484	3.0-3.5	.078	.030	.033	.003	.003	.147
3.5-4.0	.164±.029			3.5-4.0	.068	.028	.030	.003	.002	.131
4.0-5.0	.361±.101			4.0-5.0	.057	.027	.027	.002	.002	.115
				5.0-6.0	.045	.025	.023	.002	.001	.096

4.3.3 Monte Carlo for π^0, η, η' and ω Direct Photon Backgrounds

The contributions of π^0 decays to the direct photon background were determined by generating decays with a uniform distribution in p_T, rapidity and azimuth throughout the region of space occupied by the detector. The photons in each π^0 decay were required to land at least 5 cm from each edge of the detector. Both photons in each decay were also required to have an energy greater than 1 GeV. In decays where one photon failed the above requirements the accepted photon was designated as a background single photon. Each generated π^0 and any resulting background single photon from the π^0 decay was tested for acceptance within the fiducial limits in p_T, rapidity and vertical position given in Table 4.2. For each generated π^0 a weight proportional to the fitted value of the π^0 inclusive cross section (presented in Section 4.2.6) at the p_T of the generated π^0 was calculated $(2\pi p_T \exp(\alpha+\beta p_T))$. This weight was applied to each accepted π^0 and any accepted background single from the π^0 decay. The resulting "inclusive" background single distribution was then divided by the weighted π^0 distribution to produce the background to the direct-photon to π^0 ratio given in Table 4.5 under the heading $\pi^0("\gamma"/\pi^0)$.

In an analogous procedure an equal number of η decays were generated using the η cross section given in Section 4.2.6. However, in this case the "inclusive" background single photon distribution was divided by the weighted π^0 distribution described above. The resulting "γ"/π^0 ratio was then weighted by the .39 branching ratio for the

electromagnetic decay of the η and given in Table 4.5 under the heading η ("γ"/π⁰).

Estimates on the production ratios of η'/π^0 and ω/π^0 were used (0.90±0.25 and 0.44±0.08 respectively) to generate η' and $\omega \rightarrow \pi^0 + \gamma$ decays in the manner described for the π^0 and η above.[32] These decays were analyzed in the same way as the π^0 and η decays to provide the upper limits on the "γ"/π⁰ background given in Table 4.5 under the η'("γ"/π⁰) and ω^0("γ"/π⁰) headings.

4.3.4 Monte Carlo for the Charged Hadron Direct Photon Background

Approximately equal production of π^0, π^+ and π^- has been observed.[33] Based on these results the π^0 cross sections given in Table 4.4 can be used as an approximation to the π^+ and π^- cross sections.

The LAC presented a 1.2 absorption length to pions (see Section 2.1.3). This implies that 70% of all charged pions that entered the LAC interacted and deposited energy. As noted in Section 3.2.3 any candidate photon which deposited more than half of its energy in the back half of the detector was rejected as being a probable hadron. However, there was no rejection of hadrons which interacted in the front of the detector and deposited more than 50% of their energy there. To estimate the contamination to the direct photon signal due

to this source a model was derived from E272 data in which charged pions hitting the LAC were independently measured with a magnetic spectrometer. The usage of the LAC in E272 is described elsewhere.[26] Analysis of this data determined that the distribution in the fraction $E(total)/E_\pi$ where E(total) is the energy deposited in the LAC by a charged pion of energy E_π was independent of the pion energy. This distribution was fit to a low order polynomial in the region where the fraction exceeded 0.5. Similarly, the distributions of $E_{(back)}/E_{(total)}$ where both are deposited energies, were fit to a low order polynomial in several ranges of $E_{(total)}/E_\pi$ in the region $E_{(back)}/E_{(total)}$ greater than 0.5. The distributions of $E_{(back)}/E_{(total)}$ showed that between 49% and 67% of interacting hadrons (depending on the total energy fraction) deposited more than half of their energy in the front of the LAC which would allow them to pass the hadron rejection described in Section 3.2.3. With the parameterizations of the various distributions it was then possible to use the π^0 cross sections given in Table 4.4 to generate a inclusive distribution of π^+ and π^- and predict how many charged pions would appear as photons within the fiducial limits described in the previous sections. The resulting p_T spectrum was compared to the inclusive p_T spectrum for π^0s used in Section 4.3.3 to provide the estimate of "γ"/π^0 due to charged pions. A upper limit on charged hadron contamination was obtained by rescaling the charged pion contamination by the sum of the production ratios of $K^{+\backslash-}$,$p/\bar{p}$ and $n/\bar{n}$ to π^+ or π^-. This results in a factor of 2.0 due to the 2 species of charged pion, 0.53+0.17 from Kaons and 1.11+0.03 from Protons and Neutrons.[34] The upper limit on charged hadron contamination is then 3.84 times the

estimate for charged pion contamination and is given under the charged hadron ("γ"/π^0) heading in Table 4.5.

Chapter 5

Final Results and Conclusions

In this chapter the π^0, η and Direct Photon inclusive production cross sections for p and π^+ beams interacting in carbon targets will be presented. Comparisons with world data will be discussed.

5.1 π^0 and η Inclusive Production Cross Sections

The π^0 and η cross sections listed in Table 4.4 for incident p and π^+ are presented in in Figures 5.1. Within experimental errors, the π^0 and η cross sections have the same p_T dependence. The ratio of η to π^0 production averaged over all the data on carbon is $\eta/\pi^0 = 0.49 \pm 0.03$, which is consistent with recent measurements at large p_T on hydrogen[35] and on beryllium[36] at 200 GeV/c. The production ratio of π^0 to η for p-C at 2.89 GeV/c is 0.538 ± 0.052. Measurements of K^+/π^+ at 200 GeV/c report ratios of 0.42 ± 0.02 for p-p , $0.487 \pm .010$ with p-W, 0.489 ± 0.009 with p-Ti and 0.462 ± 0.029 with p-Be all at 3.08 GeV/c p_T.[33] All but the p-p data compare within experimental error indicating an approximately equal production of K^+ and η at large p_T.
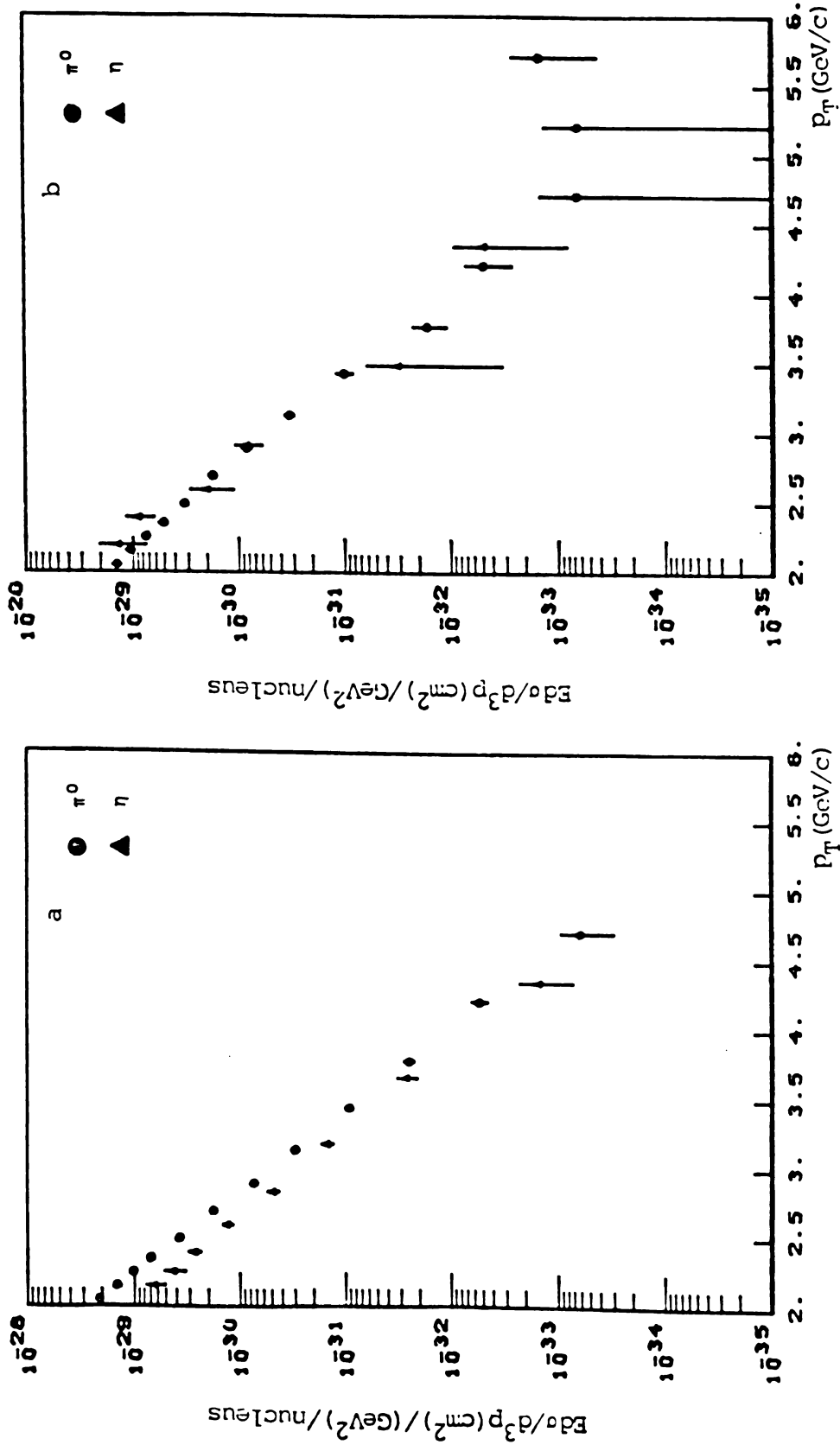
Figure 5.1; π^0 and η invariant cross sections at 200 GeV/c taken with a carbon target in the center-of-mass rapidity interval (-.8 to .2) a) for incident p and b) for incident π^+.

One of the earliest indications that large-p_T production could be related to hard scattering of constituents was provided by Donaldson et al.,[37] in their observation of an increased yield of π^0s at large p_T in π^+p relative to pp collisions. This increase was attributed to the higher probability of finding a large-x valence quark in the structure function of a pion. The results shown in Figure 5.2 indicate a similar effect in interactions on a nuclear target (carbon). This suggests that any rescattering which occurs in the nuclear targets does not obscure the differences observed in meson production from the hard interactions of pions and protons on single nucleons.

5.2 γ/π^0 and Direct Photon Inclusive Production Cross Section

The ratio of single photons to the inclusive π^0 yield listed in Table 4.5 under the "data (γ/π^0) " heading is shown for proton and π^+ beams in Figures 5.3a and 5.3b respectively.

The data have been integrated over c.m. rapidities between -0.75 and +0.2. Also shown are the background contributions to the ratio expected from the undetected π^0 and η decays, ω^0 and η' decays, and hadron contamination listed in Table 4.5. Typically, the π^0 and η decays constitute, respectively, 56% and 19% of this background. Below a p_T of 2.5 GeV/c the data are consistent with contributions expected from the background. For $p_T>3.0$ GeV/c the data are consistently above the level expected from the background. The inclusive cross sections
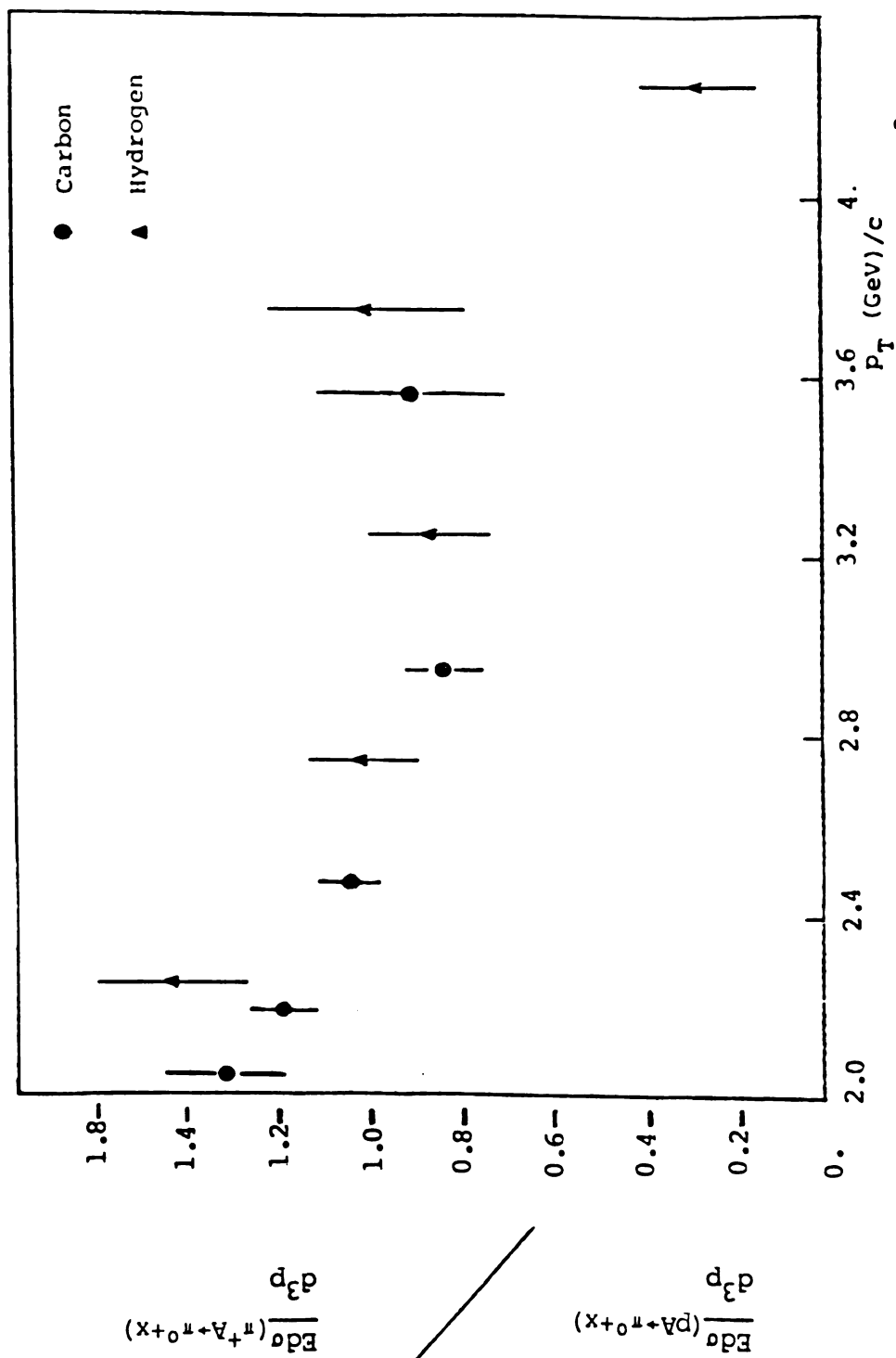
Figure 5.2; Ratio of invariant cross sections $Ed\sigma(pA \rightarrow \pi^o + x)/d^3p$ and $Ed\sigma(\pi^+A \rightarrow \pi^o + x)/d^3p$ vs p_T for A = carbon and A = hydrogen at 200 GeV/c , hydrogen data are from Donaldson et al., 1976.[3]
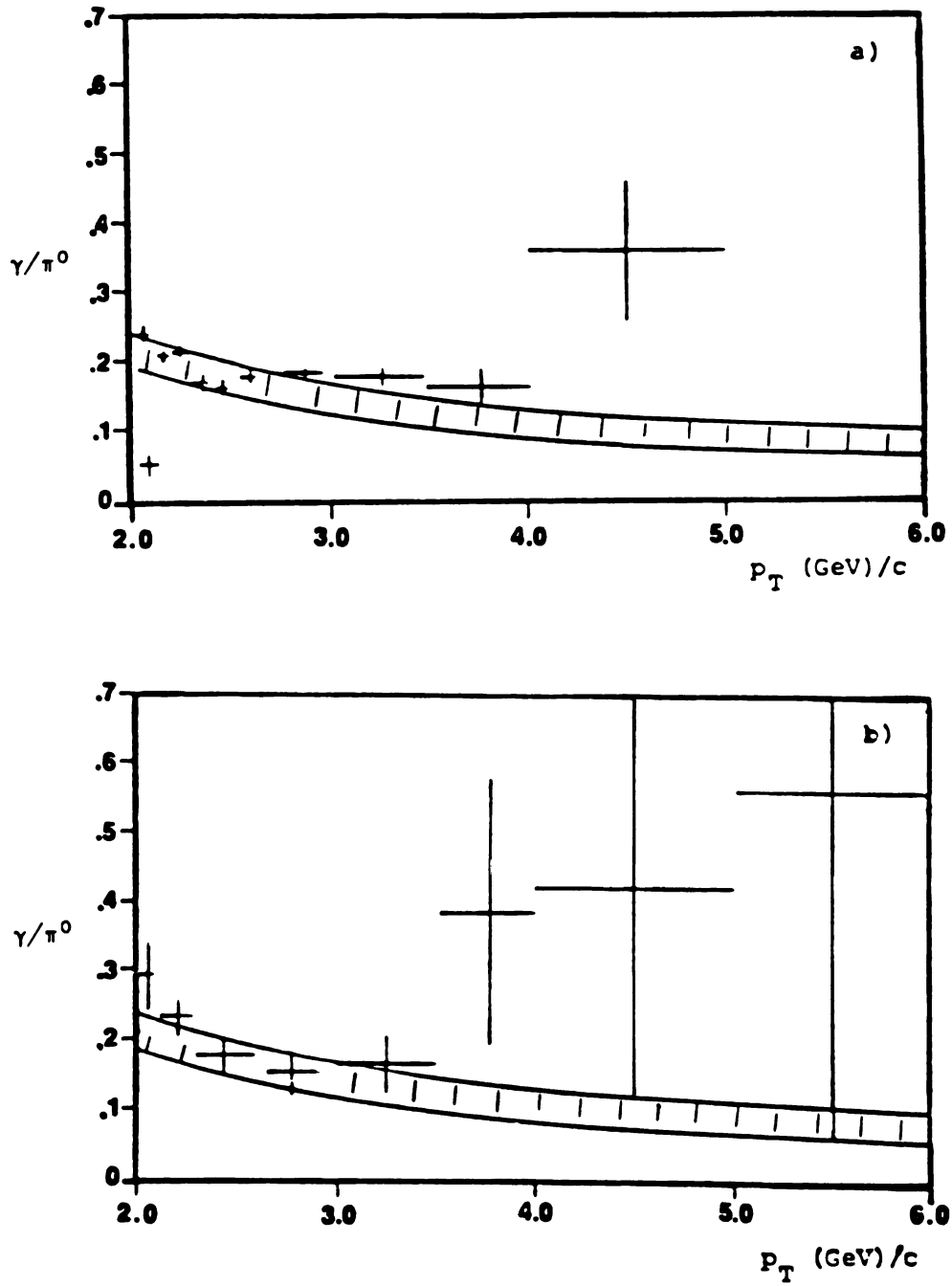
Figure 5.3; Inclusive (direct photon + background) to π^0 ratio at 200 GeV/c with a carbon target in the center-of-mass rapidity interval (-.80 to .2) a) for incident p b) for incident π^+, shaded bands are background estimates.

for direct-photon production computed from the inclusive γ/π^0 and π^0 inclusive cross sections after subtraction of the γ/π^0 background are given in Table 5.1. It is important to emphasize that these are inclusive measurements; no restrictions have been placed on the associated event structure. In fact, most of the single-photon and π^0 triggers above a p_T of 2.5 GeV/c consist of isolated showers with little if any additional electromagnetic activity within the acceptance region of the photon detector.

In the following paragraph comparisons will be made to other measurements.[38]

These results are in reasonable agreement with a previous measurement of the γ/π^0 ratio at Fermilab (Baltrusaitis et al.[36]) of γ/π^0 =0.05-0.09 in pBe→γX, for p_T>3 GeV/c. However, at smaller values of transverse momentum (p_T<2.5 GeV/c) the data presented here show an upper limit for γ/π^0 of 0.02; this result is well below that of the previous measurement. The results presented here are more consistent with those obtained at the CERN intersecting storage rings (ISR), where measurements of direct photons[39] and of low-mass virtual photons (e$^+$e$^-$ pairs)[40] indicate several-percent upper limits for the γ/π^0 ratio in the p_T range of 2-3 GeV/c, and a subsequent rapid rise of that ratio with increasing p_T. The measurements of Amaldi et al.[39] in the p_T range of 3-4 GeV/c at $\sqrt{s}$=51 GeV are consistent with the value of γ/π^0=0.03 that is found here for $\sqrt{s}$=19.4 GeV. The value of 0.03 is just below but within systematic error of the measurements of Diakonou et al.[39] in the same p_T range but at at $\sqrt{s}$=31 GeV. Theoretical estimates for γ/π^0 are about a factor of 2 below the results presented here.[41]

Table 5.1; Inclusive γ/π^0 and $Ed\sigma(\gamma)/d^3p$/nucleon (cm^2/GeV^2).

P_T(GeV)/c	Incident Proton γ/π^0	$Ed\sigma(pC\to\gamma+X)/d^3p$	P_T(GeV)/c	γ/π^0	$Ed\sigma(\pi^+C\to\gamma+X)/d^3p$
2.0-2.1	.009±.012		2.0-2.1	.063±.053	
2.1-2.2	<.025		2.1-2.3	.026±.029	
2.2-2.3	.009±.011		2.3-2.5	<.044	<1.60X10^{-32}
2.3-2.4	<.014	<1.45X10^{-32}	2.5-2.7	<.028	<5.88X10^{-33}
2.4-2.5	<.020	<7.44X10^{-33}	2.7-3.0	.016±.028	(1.31±2.29)X10^{-33}
2.5-2.7	.008±.010	(1.70±2.13)X10^{-33}	3.0-3.5	.010±.032	(2.07±6.63)X10^{-34}
2.7-3.0	.014±.010	(1.10±0.79)X10^{-33}	3.5-4.0	.263±.189	(5.16±3.96)X10^{-34}
3.0-3.5	.037±.013	(6.90±2.44)X10^{-34}	4.0-5.0	.306±.286	(7.29±7.48)X10^{-35}
3.5-4.0	.033±.029	(8.94±7.89)X10^{-35}	5.0-6.0	.487±.484	(4.42±5.09)X10^{-35}
4.0-5.0	.246±.101	(6.25±2.74)X10^{-35}			

It is useful to note that the results for the γ/π^0 ratio are similar in both the proton and π^+ data. In view of the predicted dominance of the u-quark (see Section 1.4) Compton process for photons in this range of p_T, only small differences in the ratio would have been expected.

The scaling behavior of inclusive photon production with energy was investigated by comparing this data with the measurements from the ISR that have the most reliable absolute normalization.[42] A fit to the form $C(1-x_T)^M p_T^{-N}$, where C is a normalization factor, yielded values of $M=10.1\pm0.7$, $N=6.2\pm0.2$, and $C=(3.4\pm1.4)\times10^{-29}$ cm^2/GeV^2. Effects from uncertainty in the relative normalization of the two experiments have been included in the errors.

The cross section data multiplied by $p_T^{6.2}$ are compared to the fitted function in Figure 5.4. Plotted this way the data at the two energies do seem to display a purely x_T dependence. The fitted value of $N=6.2$ is significantly lower than the corresponding value of $N=8$ found for π^0 production, but larger than the value $N=4$ expected in naive parton models and close to the value of $N=5.3$ found for jet production at the ISR and SPS.[17]

In conclusion a clear signal for direct-photon production in both pC and π^+C collisions for $p_T>3.0$ GeV/c has been observed. The γ/π^0 ratio at fixed p_T appears to be nearly energy independent between $\sqrt{s}=19.4$ GeV and $\sqrt{s}=63$ GeV. Finally, the inclusive photon yield has a p_T dependence that is close to the form observed for production of

Figure 5.4; Fit to E629 and R806 data[42] to a function of p_T and x_T
$$E d\sigma/d^3p = (34 \pm 14)(1-x_T)^{10.1 \pm 0.7} p_T^{-6.2 \pm 0.2} \, \mu b/GeV^2.$$
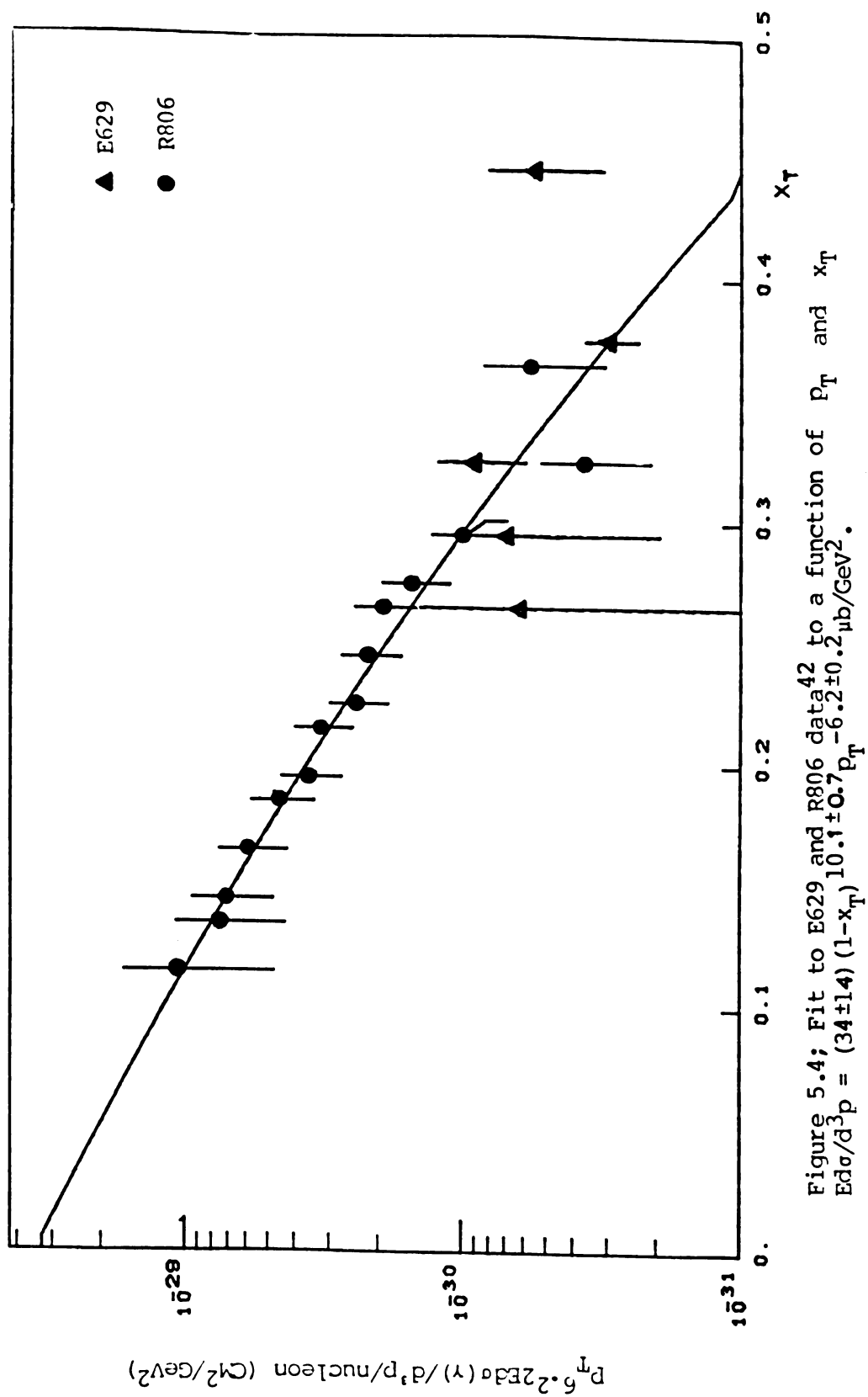
constituent jets at the ISR, as would be expected on the basis of the kind of diagrams shown in Figures 1.2b and 1.2d.[43]

APPENDICES

Appendix A

LAC Fast Outputs

a) Timing

High energy photons dissipate energy in the LAC through the formation of electron positron pairs which lose energy by ionization of the material in the calorimeter. The number of ion pairs formed in electromagnetic showers is therefore proportional to the energy of the photon.

When ionization occurs in a LAC cell (see Figure A.1a) the observed current is given by

$$i(t) = Ne(1-t/t_d)v_d/d$$

where N is the number of ion pairs, v_d is the drift velocity, e is electron charge and t_d is the time required for a charge to cross a cell of width d.[23] In the experiment charge sensitive amplifiers were use to process LAC signals. The amplifiers produced a voltage V proportional to charge where

$$V_{amp} \propto Ne(t/t_d - t^2/2t_d).$$

It is important to note that this voltage is directly proportional to N the number of ion pairs which, as noted above, is directly proportional to the energy (E) of the photon. The voltage for the fast outputs of the LAC, which are used for timing, rise linearly for short times $(t \leq t_d/2)$ as
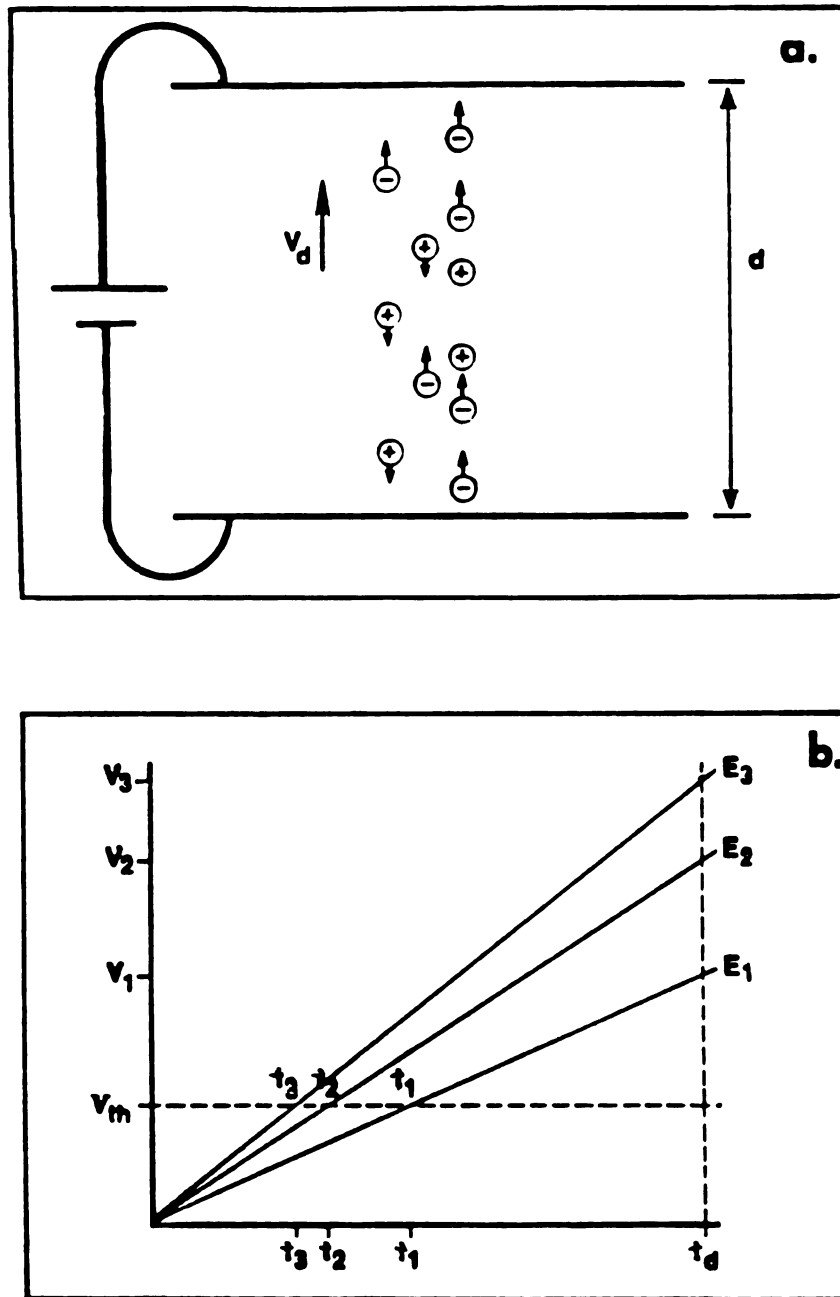
$$V_{amp} \propto Net/t_d \propto Et/t_d.$$

Figure A.1; a) Ionization in a single LAC cell b) pulse height vs
time for energies $E_1 < E_2 < E_3$.

Low threshold discriminators on the fast outputs provided the stop signals for TDC's (Time to Digital Converters) initiated by the pre-trigger described in Section 2.6.1. The time for a signal to come above a given threshold (see Figure A.1b) is proportional to V_{th} where V_{th} is the discriminator threshold voltage and inversely proportional to energy. Operationaly the LAC thresholds varied from channel to channel and delay times due to differing signal cable lengths and amplifier responses resulted in a two parameter model for the timing of each strip,

$$t_i = a_i + b_i/E$$

where a_i is the offset, b_i accounts for differences in TDC discriminator thresholds and E is the energy deposited in the strip.

b) Capacitive Effects in the LAC

The experimental trigger which utilized the sum of the amplifier fast outputs was subject to capacitive distortions. The source of these distortions will be evaluated using a simplified model of the LAC shown in Figure A.2. Two LAC signals, s_1 and s_2 are amplified and summed. The low mobility of positive ions relative to that of electrons results in a net positive charge remaining at LAC strip 1 after all the electrons have been collected. This positive charge induces an image in the negative high voltage plate (lead conversion sheets in the physical LAC) which results in a signal of opposite sign in strip 2. The presence of a ballast capacitance (C_b) prevents the real signal due to ionization in strip 1 from being cancelled by the induced signal in strip 2. Image charge effects are kept within
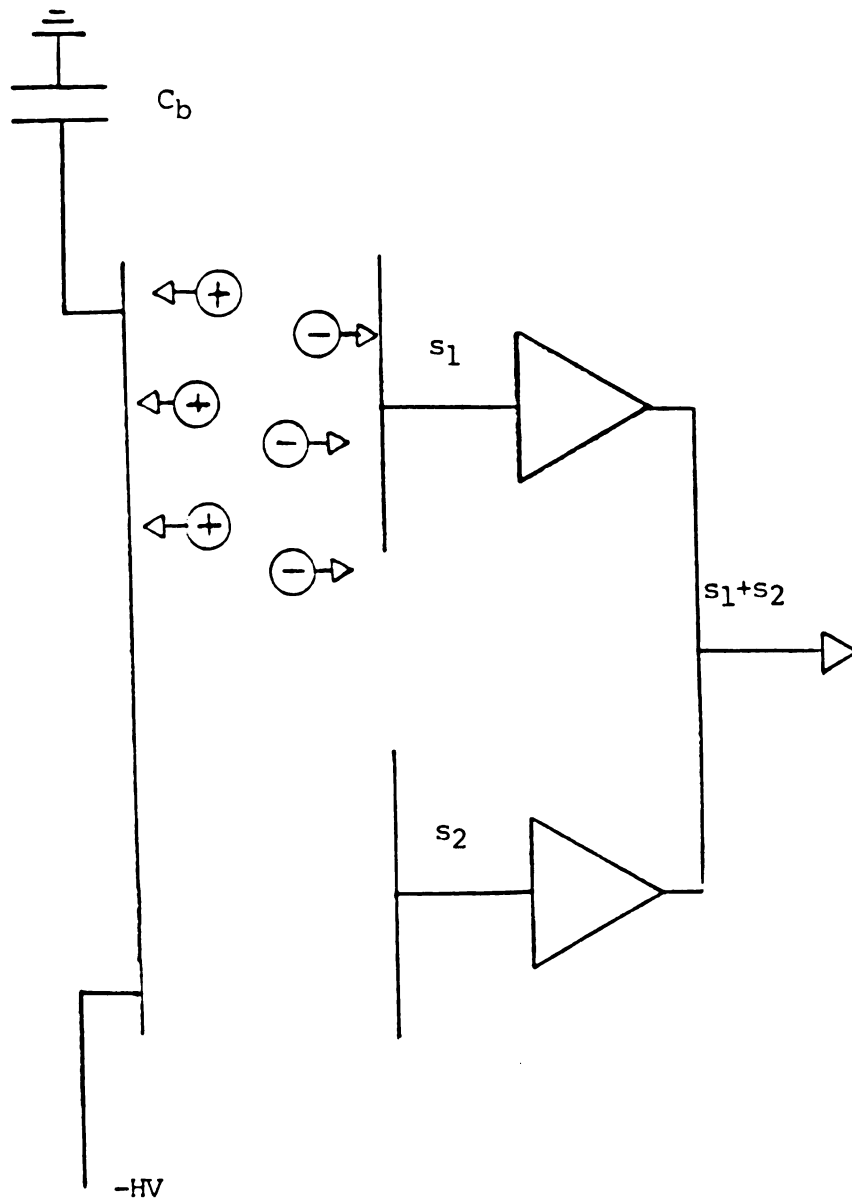
Figure A.2; Signal formation in a simple LAC model.

manageable limits by minimizing the ratio of detector to ballast capacitance. This ratio was approximately 1/3 for the LAC used in this experiment.

c) P_{Tx} Trigger Model

To compensate for the image charge effect just described a modified weighting of the individual strip energies where the strips are the anodes of the LAC cells was used to achieve a P_{Tx} trigger. Referring again to Figure A.2 the same voltage drop appears across both the ballast capacitance (C_b) and the effective capacitance (C_d) of the detector. As a result in this simple model of a LAC the charge $(Q_i = Q_{b_i} + Q_{d_i})$ collected from the ionization at any given strip (i) will ultimately come from the ballast (C_b) and detector (C_d) capacitance in the ratio $\gamma = Q_d/Q_b = C_d/C_b \approx 1/3$. Any charge Q_{d_i} drawn from the capacitance of the detector at one strip will appear as a image charge $-Q_{d_i}$ collected from the other strips in the detector. As noted earlier the energy deposited in a given strip (E_i) is directly proportional to the amount of ionization appearing at the strip. This ionization is collected as

$$Q_{strip} = Q_i - \gamma Q/(1+\gamma)n$$

where $Q = \sum_i Q_i$ and n is the total number of strips in the summation.

The direct proportionality relationship between ionization and deposited energy results in

$$E_{strip} = E_i - E/4n$$

where $(\gamma/(1+\gamma)=1/4)$ and $E = \sum_i E_i$.

The trigger was formed by giving each x-strip a weight w_i and summing over all strips to produce

$$T = \sum_i E_i (w_i - \overline{w}/4).$$

For our detector a weighting of

$$w_i = \sin\theta_i + 0.051$$

recovers a transverse momentum trigger

$$T = P_{Tx} = \sum_i \sin\theta_i.$$

The correction to $\sin\theta$ weighting that was actually used varied from 0.081 on the away side of the detector to 0.057 on the beam side of the detector which resulted in an approximately constant yield of events across the detector (see Section 3.3.1). With this weighting $\overline{w}/4=0.051$ which compares with the value of 0.067 derived from the data as described in Section 3.3.2.

Appendix B

LAC Trigger Efficiency (p_T)

The simplest model for p_T trigger turn-on is illustrated by Figure B.1a. At p_T values below the threshold (λ) the trigger is completely off and for values at or above λ the trigger is 100% efficient. However, to account for variations of measured p_T from actual p_T due to the resolution of the detector and electronic noise a more complicated model for the trigger turn-on is required. One possible procedure is to assume that the measured p_T varies from the actual p_T according to a Gaussian distribution (represented by the bell shaped curve in the figure). In this model the probability of a given event of $p_T = P$ being above threshold is

$$\text{probability} = \int_{P-\lambda}^{\infty} G(p_T) \, dp_T, \text{ where}$$

$$G(p_T) = \frac{1}{\sigma\sqrt{2\pi}} \exp[-(p_T-\lambda)^2/2\sigma^2].$$

The effective trigger efficiency (turn-on) as a function of p_T is then

$$\text{efficiency}(p_T) = .5[1.-\text{erf}(p_T-\lambda),\sigma]$$

where $\text{erf}(p_T-\lambda) = (2/\sqrt{\pi})\int_0^{p_T-\lambda} \exp[-(p_T-\lambda)^2/2\sigma^2]dp_T$. The effect of this trigger resolution "smearing" is shown in Figure B.1b where the trigger turn-on is shown for Gaussian "smeared" p_T (curve with point of inflection at λ). The trigger turn-on for the "sharp" threshold (step function) is shown for comparison. For $\sigma \to 0$ the "smeared" trigger converges to the step function. At the nominal threshold of λ the efficiency for the smeared trigger is 50%.
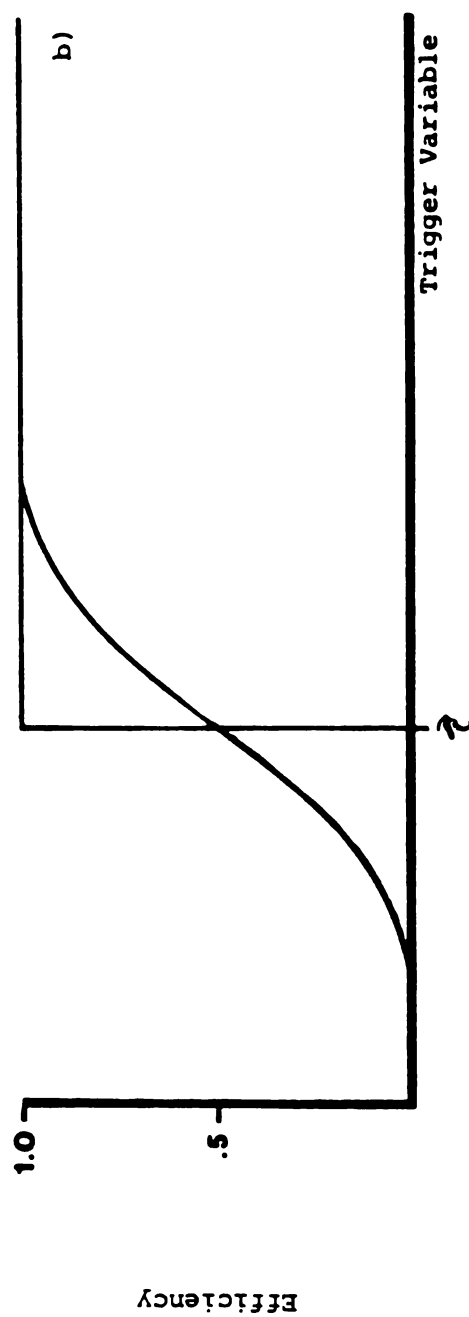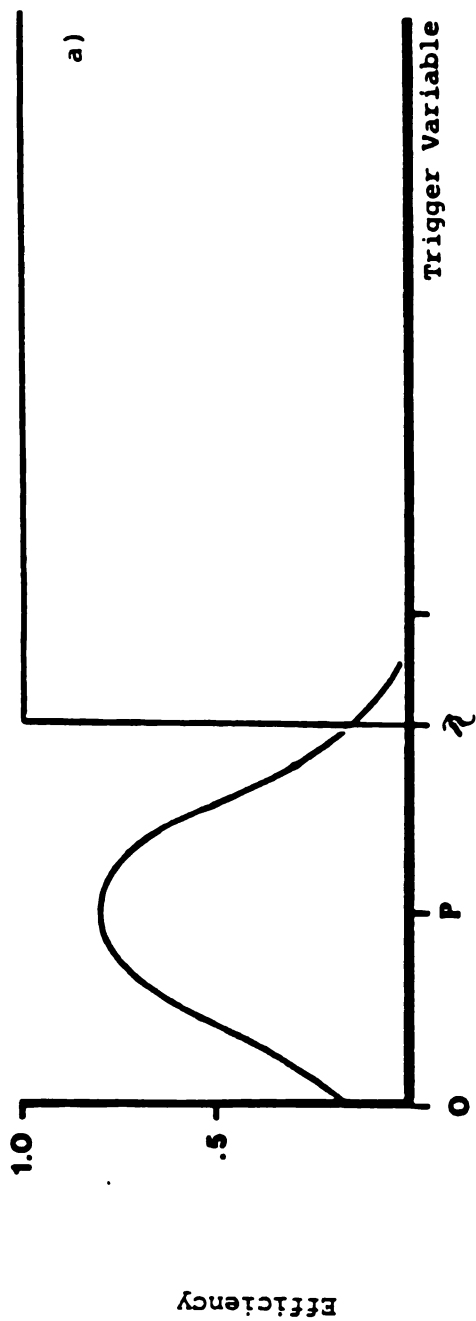
Figure B.1: Trigger turn-on a) step function trigger for an event with Gaussian smearing about P b) Gaussian spreading of the trigger turn-on.

Appendix C

E629 Variables and Lorentz Kinematics

a) Meson $\gamma\gamma$ Decay

For the decay of meson $\rightarrow \gamma\gamma$ a straightforward application of the Lorentz transformation and some algebra yields a useful relationship between the lab (measured) energies of the decay photons E_1 and E_2, and the angle θ^* between the meson center of mass (CM) decay axis and lab momentum axis

$$\underline{\text{Asymmetry}} = (E_2-E_1)/(E_2+E_1) = \beta\cos\theta^*.$$

Due to the $\cos\theta^*$ term, a meson with an isotropic decay will have a flat asymmetry distribution in the CM.

b) Lab Opening Angle

Comparison of the scaler products of the meson 4-momentum in the CM and the sum of the 4-momenta of the decay photons in the LAB yields the following relationship

$$\cos\theta = 1-2/[1+\frac{P^2}{m^2}(1-\cos^2\theta^*)]$$

where P is the meson momentum and θ is the angle between the 3-momenta of the decay photons in the lab frame. For fixed P and m, a minimum is obtained for θ when $\theta^*=\pm\pi/2$ radians, while a maximum of $\theta=\pi$ radians is obtained when $\theta^*=\pm\pi$ radians. Also, for fixed P and θ' a increase in the meson mass m will result in a increase in the minimum θ.

c) Rapidity

The standard Lorentz invariant differential volume element in momentum 3-space is d^3P/E.

However, when the Lorentz invariant variable of interest is p_T, $Ed^3\sigma/d^3P = f(P_1,P_2,P_3)$ is awkward. A more useful parameterization can be formed with the variables p_T and rapidity (y) where

$$y = .5 \ln[(E+P_L)/(E-P_L)]$$

with P_L being the component of momentum parallel to the rapidity (Lorentz boost) axis. Application of the Jacobian

$$dp_Tdy = \det[\partial(p_T,y)/\partial(P,\theta)]dPd\theta$$

yields

$$d^3P/E = 2\pi p_T dp_T dy.$$

This results in the parameterization

$$d\sigma/2\pi p_T dp_T dy = f(p_T,y)$$

where p_T is Lorentz invariant and $y(\text{Lor. trans.}) \rightarrow y - .5\ln[(1-\beta)/(1+\beta)]$. With this parameterization $f(p_T,y)$ has the same distribution in p_T and the same shaped distribution in y under all Lorentz transformations parallel to the rapidity axis.

Appendix D

Experimental Determination of Invariant Differential Cross Sections

The Lorentz invariant differential cross section is given by

$$E\frac{d\sigma}{d^3p} = \frac{d\sigma}{2\pi p_T dp_T dy}$$

where y is rapidity.

If a total of N_0 particles strikes a target of density ρ nucleons per cm^2, a total production of

$$N = N_0 2\pi p_T \Delta p_T \Delta y \frac{d\sigma}{2\pi p_T dp_T dy}$$

will be observed within the ranges of Δy and $p_T \pm \Delta p_T/2$ in rapidity and p_T. Experimentaly the differential cross section becomes for N observed events about a given p_T within a given rapidity range

$$\frac{d\sigma}{2\pi p_T dp_T dy} = \frac{N}{2\pi N_0 \rho p_T \Delta p_T \Delta y}.$$

LIST OF REFERENCES

LIST OF REFERENCES

1) James D. Bjorken and Sidney D. Drell, Relativistic Quantum Mechanics, (McGraw-Hill Book Co.,1964); idem., Relativistic Quantum Fields,(McGraw-Hill Book Co.,1965).

2) Francis Halzen and Alan D. Martin, Quarks and Leptons: An Introductory Course in Modern Particle Physics, (John Wiley and Sons,(1984).

3) H. D. Politzer, Phys. Rev. Lett. 30, (1973) 1346; D. Gross and F. Wilczek, Phys. Rev. Lett. 30, (1973) 1343.

4) L. W. Jones, Rev. Mod. Phys. 49, (1977) 717.

5) D. Sivers, S. J. Brodsky and R. Blankenbecler, Phys. Rep. 23C, (1976) 1;

6) R. D. Field and R. P. Feynman, PhYs. Rev. D 15, (1977) 2590.

7) See Reference 2, Section 9.4.

8) Elliot Leader and Enrico Predazzi, An Introduction to Gauge Theories and "New Physics", (Cambridge University Press,1982).

9) See Reference 2, Section 9.3; See Reference 6, Section II.

10) V. E. Barnes, et al., Phys. Rev. D 25, (1982) 1.

11) S. L. Glashow, J. Iliopoulos, and L. Maiani, Phys. Rev. D 2, (1970) 1285; J. J. Aubert, et al., Phys. Rev. Lett. 33, (1974) 1404; Makoto Kobayashi and Toshihide Maskawa, Prog. Theor. Phys. 49, (1973) 642; J. Ellis, M. K. Gaillard, D. V. Nanopoulos and S. Rudaz, Nuc. Phys. B 148, (1977) 285.

12) S. M. Berman, J. D. Bjorken and J. B. Kogut, Phys. Rev. D 11, (1971) 3388.

13) D. Cline, F. Halzen and M. Waldrop, Nucl. Phys. B 55, (1973) 157.

14) R. Rückl, S. J. Brodsky and J. F. Gunion, Phys. Rev. D 18, (1978) 2469; F. Halzen and D. M. Scott, Phys. Rev. D 18, (1978) 3378.

15) H. Fritzsch and P. Minkowski, Phys. Lett. 69B, (1977) 1316; G. Farrar, Phys. Lett. 67B, (1977) 337.

16) A. P. Contogouris, S. Papadopoulos and M. Hongoh, Phys. Rev. D 19, (1979) 2607.

17) C. De Marzo, et al., Phys. Lett. 112B, (1982) 173.

18) Åkesson, et al., Phys. Lett. 118B, (1982b) 185; Åkesson, et al., Phys. Lett. 118B, (1982b) 193; Banner, et al. , Phys. Lett. 118B, (1982) 203; Åkesson, et al., Phys. Lett. 123B, (1983a) 133.

19) L. Cormell and J. F. Owens, Phys. Rev. D 22, (1980) 1609.

20) M. Nowak and M. Praszalowicz, Z. Phys. C 17, (1983) 249.

21) J. Povlis, et al. , Phys. Rev. Lett. 51, (1983) 967.

22) C. Bromberg et al., Nucl. Inst. and Meth. 200, (1982) 245.

23) W. J. Willis and V. Radeka, Nucl. Instr. and Meth. 120, (1974) 221; C. Fabjan et al., Nucl. Instr. and Meth. 141, (1877) 61; J. H. Cobb et al., Nucl. Instr. and Meth. 158, (1979) 93; D. Hitlin et al., Nucl. Instr. and Meth. 137, (1976) 225; G. Knies and D. Neuffer, Nucl. Instr. and Meth. 129, (1974) 1.

24) T. F.Droege, F. Lobkowicz and Y. Fukushima, Fermilab Report TM-746 2500.000 (Oct. 1977).

25) Michael R. Mclaughlin, Ph.D. dissertation, University of Rochester (1983) 92-97.

26) C. Nelson et al., Nucl. Inst. and Meth. 216, (1983) 381.

27) E. Anassontzis et. al. Z. Phys. C 13, (1982) 277.

28) See Reference 25 pages 68-73.

29) See Reference 25 pages 74-80.

30) See Reference 26 for a description of Fermilab experiment E272 from which this data was obtained.

31) See Reference 25 pages 81-88

32) G. J. Donaldson, et al., Phys. Rev. D 21, (1980) 828; M. Diakonou, et al., Phys. Lett. B 89, (1980) 432.

33) D. Antreasyan, et al., Phys. Rev. D 19, (1979) 764.

34) J. W. Cronin, et al., Phys. Rev. D 11, (1975) 3105. The factor of 1.11 assigned to proton + neutron contamination is obtained by

assuming equivalent production for protons and neutrons and a upper limit of 50% on the effectiveness of both in converting a large fraction of their energy into electromagnetic showers when compared to π^+ and π^- which can do so by charge exchange interactions $\pi^+ n \rightarrow \pi^0 p$ and $\pi^- p \rightarrow \pi^0 n$. V. Böhmer et al., Nucl. Inst. and Meth. **122**, (1974) 313. These results show a 1.1/1.0 deposited energy ratio for π^+ relative to p in a 33 radiation length absorption calorimeter. However, the p data consist of a 50% sample of protons whose showers were confined in the detector indicating a greater likelihood for π^+'s to mimic photon showers than for p's.

35) G. Donaldson et al., Phys. Rev. Lett. **40**, (1978) 684.

36) R. M. Baltrusaitis et al., Phys. Lett. **88B**, (1979) 372.

37) G. Donaldson et al., Phys. Rev. Lett. **36**, (1976) 1110.

38) T. Ferbel and W. Molson, Rev. Mod. Phys. **56** 2, (1984) 181;

39) E. Amaldi et al., Nucl. Phys., B **150**, (1979) 326;
J. Cobb et al., Phys. Lett. **78B**, (1978) 519 M. Diakonou et al., Phys. lett. **91B**, (1980) 296;
A. Angelis et al., Phys. Lett. **94B**, (1980) 106, and **98B**, (1981) 115.

40) J. Cobb et al., Phys. Lett. **78B**, (1978) 519.

41) S. Petrarca and F. Rapauno, Phys. Lett. **88B**, (1979) 167;
F. Halzen, M. Dechantsreiter, and D. M. Scott, Phys. Rev. D **22**, (1980) 1617;
A. P. Contogouris, A. Papadopoulos, and J. Ralston, Phys. Lett. **104B**, (1981) 70 and Phys. Rev.D **25**, (1982) 1280;
R. Baier, J. Engels, and B. Petersson, Z. Phys. C **6**, (1980) 309;
reference 14, R. Rückl, S. J. Brodsky and J. F. Gunion;
reference 19.

42) E. Anassontzis et al., Z. Phys. C **13**, (1982) 277. this is in chap2
These are essentially the results of the experiment of Diakonou et al., Ref. 37, multiplied by a factor of approximately 1.4 to correct the measurements to inclusive yields. Also see V. Burkert's study of the scaling properties of direct-photon production, in Proceedings of the Eighteenth Rencontre de Moriond, Les Arcs, France, 1983, edited by J. Tran Thanh Van (to be published); and J. Huston, in Proceedings of the Colloquium on Multiparticle Dynamics, Lake Tahoe, 1983, edited by J. Gunion (to be published).

43) W. Molzon, in Proceedings of the Eighteenth Rencontre de Moriond, Les Arcs, France, 1983, edited by J. Tran Thanh Van (to be published).